



**CATHODOLUMINESCENCE AND PHOTOEMISSION OF DOPED LITHIUM
TETRABORATE**

THESIS

Christina L. Dugan, Major, USA

AFIT/GNE/ENP/11-M05

**DEPARTMENT OF THE AIR FORCE
AIR UNIVERSITY**

AIR FORCE INSTITUTE OF TECHNOLOGY

Wright-Patterson Air Force Base, Ohio

APPROVED FOR PUBLIC RELEASE; DISTRIBUTION UNLIMITED

The views expressed in this thesis are those of the author and do not reflect the official policy or position of the United States Air Force, Department of Defense, or the United States Government. This material is declared a work of the U.S. Government and is not subject to copyright protection in the United States.

AFIT/GNE/ENP/11-M05

**CATHODOLUMINESCENCE AND PHOTOEMISSION OF DOPED LITHIUM
TETRABORATE**

THESIS

Presented to the Faculty
Department of Engineering Physics
Graduate School of Engineering and Management
Air Force Institute of Technology
Air University
Air Education and Training Command
In Partial Fulfillment of the Requirements for the
Degree of Master of Science in Nuclear Engineering

Christina L. Dugan, BS

Major, USA

March 2011

APPROVED FOR PUBLIC RELEASE; DISTRIBUTION UNLIMITED

AFIT/GNE/ENP/11-M05

**CATHODOLUMINESCENCE AND PHOTOEMISSION OF UNDOPED AND MN
DOPED LITHIUM TETRABORATE**

Christina L. Dugan, BS

Major, USA

Approved:

Robert L. Hengehold, PhD (Chairman)

Date

LTC John W. McClory (Member)

Date

Yung Kee Yeo, PhD (Member)

Date

Abstract

Lithium tetraborate ($Li_2B_4O_7$) crystals are being developed for possible use in solid state neutron detectors. Already used in thermoluminescent dosimeters, enriched $Li_2B_4O_7$ is of interest due to its large cross section for neutron capture by 6Li and ^{10}B . The $^6Li(n,\alpha)^3H$ and $^{10}B(n,\alpha)^7Li$ reactions are the basis for neutron detection, and a $Li_2B_4O_7$ crystal enriched with Mn should show improved efficiency for neutron detection. $Li_2B_4O_7$ crystals doped with Mn significantly increases the light output in dosimeter applications. There is, however, a lack of fundamental characterization information regarding this useful material, particularly with regard to its electronic configuration.

Photoemission spectroscopy was used to determine the energy level structure of the Mn doped $Li_2B_4O_7$ crystals. Measurements were made using ultraviolet photoemission spectroscopy (UPS) at the Louisiana State University (LSU) Center for Advanced Microstructures and Devices (CAMD), using synchrotron radiation on two different beamlines. The first was the 3 m toroidal grating monochromator (TGM) beam line equipped with a 50 mm hemispherical electron energy analyzer providing a resolution of 70 mev and a photon energy range up to 95 eV. The TGM spectra confirmed the presence of Mn. The second was the normal incident monochromator (NIM) beamline equipped with a Scienta SES200 electron energy analyzer with a resolution of approximately 10 mev and a photon energy range from 24 to 32 eV to study the band gap states. Measurements were

made at elevated sample temperatures to reduce charging effects. Photoemission studies provided evidence of Mn in the bulk crystal at 47.2 eV. Valence band analysis provided the presence of surface states but no acceptor sites.

Cathodoluminescence studies were also made on undoped and Mn doped $Li_2B_4O_7$ using excitation from a Kimball Physics EMG-12 electron gun and a Horiba half-meter Spectrometer. Measurements were made at various beam energies from 5 to 10 KeV and at room temperature. Self trapped exciton emission states are evident in the undoped and Mn doped $Li_2B_4O_7$ sample ranging in energies from 3.1 to 4.1 eV.

To my Mom and Dad

Acknowledgments

First and foremost I would like to thank God, for with God nothing shall be impossible. God truly blessed me with a great advisor and thesis committee, wonderful lab technicians, and loving parents. Without the assistance of the following personnel, none of this would have been possible. I would like to show my sincere gratitude to my faculty advisor, Dr. Robert Hengehold, for his guidance and support throughout the course of this thesis effort. His thorough understanding of cathodoluminescence and photoemission coupled with his innate ability to educate is greatly valued. I would like to thank the other two members of my committee, Dr. Yung K. Yeo and LTC John McClory for their time, advisement, and knowledge of material science. Their insight and experience was certainly appreciated. Another invaluable collaborator is Dr. Yaroslav Losovyj who kept the 3m/TGM&NIM end stations and Beam lines at the Center for Advanced Microstructure Devices at Louisiana State University operational. I would, also, like to thank the lab technicians, Greg Smith and Michael Ranft for their constant support, patience, and time. Their numerous hours they dedicated to repairing equipment, building new chambers, and troubleshooting are much appreciated. Last but not least, I would like to thank my parents, who support me throughout my life in all my endeavors.

Christina L. Dugan

Table of Contents

	Page
I. Abstract	iv
II. Acknowledgments.....	vii
III. Table of Contents	viii
IV. List of Figures	x
V. List of Tables	xiii
VI. Introduction.....	1
Background	1
Research Focus	3
Li ₂ B ₄ O ₇ Structure	3
VII. Theory	7
Band Gap Theory	7
Cathodoluminescence Synopsis	8
Electron Energy Disposition	12
Photoemission Spectroscopy	18
Surface States	21
VIII. Literature Review.....	25
History.....	25
Overview	25
Background Research on Li ₂ B ₄ O ₇	26
IX. Methodology	33
Cathodoluminescence	34
Photoemission Spectroscopy	41
The Photoemission Spectroscopy System.....	43
Source.....	44
3-m NIM Instrumentation	45

TGM Photoemission System.....	46
x. Analysis and Results	47
Chapter Overview	47
Results of Simulation Scenarios	47
Crystal Charging	50
Calibration of the Cathodoluminescence Systems.....	53
Cathodoluminescence Spectra of Undoped and Mn doped Li ₂ B ₄ O ₇	54
Undoped Single Crystal Li ₂ B ₄ O ₇	57
Undoped Amorphous Li ₂ B ₄ O ₇	59
Mn Doped Single Crystal Li ₂ B ₄ O ₇	61
Amorphous Mn Doped Li ₂ B ₄ O ₇	63
Photoemission Spectroscopy	66
TGM Photoemission Spectroscopy of Mn Doped Li ₂ B ₄ O ₇	67
xI. Discussion	77
Conclusion of Research	77
Recommendations for Future Research	Error! Bookmark not defined.
xII. Bibliography	80

List of Figures

Figure	Page
1. Detector Conversion Reactions [5]	3
2. Basic $[B_4O_9]^{-4}$ structural unit of $Li_2B_4O_7$ (left); orientation of B_4O_9 structural units and Li^+ ions in the crystal lattice (right) [7]	4
3. Energy Level Diagrams for Insulators, Semiconductors, and Metals [10]	8
4. Schematic diagrams of radiative transitions between the conduction band (E_c), the valence band (E_v) and the exciton (EE), donor (Ed) and acceptor levels (EA) in a semiconductor. [11]	11
5. Diagram of photoemission spectroscopy	18
6. Photoemission energy level diagram and spectrum	20
7. Echenique and Pendry view of surface states. The electron is trapped between the crystal surface and the image potential traveling back and forth between the two barriers.....	22
8. Cathodoluminescence Setup [23]	34
9. EMG-12 Electron Gun Block Diagram	36
10. Czerny-Turner spectrometer [24]	37
11. Relative Grating Efficiency for the Horiba Scientific Grating [25]	39
12. Head-On Type PMT	40
13. 3m-TGM photoemission line at CAMD	42
14. NIM photoemission line at CAMD	43
15. Preparatory, exchange, and sample chamber on the NIM line at CAMD	44
16. Center of CAMD Synchrotron Ring	45
17 (Left). CASINO model of electron penetration depth in Mn doped $Li_2B_4O_7$ with 10 KeV electron gun, 200,000 electrons, and a 10nm beam radius. (Right) Maximum electron penetration depth in Mn doped $Li_2B_4O_7$	48

Figure	Page
18. $\phi(pZ)$ curve of Mn doped $\text{Li}_2\text{B}_4\text{O}_7$ at 10 KeV with 200,000 projected electrons	49
19. Cross-section view of absorbed energy in Mn doped $\text{Li}_2\text{B}_4\text{O}_7$ sample with 10 KeV accelerating voltage	50
20. Surface of Mn doped $\text{Li}_2\text{B}_4\text{O}_7$ after cathodoluminescence. On left surface before polishing and on right the surface after polishing for thirty minutes.	52
21. Room Temperature Cathodoluminescence Spectra of Cu, Ag, Mn, and Undoped $\text{Li}_2\text{B}_4\text{O}_7$	54
22. Adiabatic potential curves for STEs in lithium borates.[30]	56
23. Cathodoluminescence spectrum of (100) $\text{Li}_2\text{B}_4\text{O}_7$ at 5,7, and 10 KeV, 50 uA of current with 400 um slit width, 1 second integration time and a -31°C PMT	58
24. Gaussian distribution of cathodoluminescence spectrum of (100) $\text{Li}_2\text{B}_4\text{O}_7$ at 5, 7 and 10 KeV, 50 uA of current with 1 second integration time, and a -31°C PMT.....	59
25. (Left) Cathodoluminescence spectrum of amorphous $\text{Li}_2\text{B}_4\text{O}_7$ at 5 and 7 KeV, 50 uA of current with 1 second integration time, and a -31°C PMT. (Right) Four peak Gaussian fit for the 5 KeV spectra at 2.2438, 2.670, 3.534, and 4.170 eV.	60
26. X-ray irradiation thermoluminescence spectra of undoped $\text{Li}_2\text{B}_4\text{O}_7$. Four peak Gaussian fit for the 5 KeV spectra at 2.573, 3.102, 3.579, and 3.993 eV.[33]	61
27. Cathodoluminescence spectrum of single crystal Mn doped $\text{Li}_2\text{B}_4\text{O}_7$ at 5 and 7 KeV, 50 uA of current with a -31°C PMT.	61
28. Cathodoluminescence spectrum of amorphous Mn doped $\text{Li}_2\text{B}_4\text{O}_7$ at 10 KeV, 50 uA of current, 400 um slit width, 1 Å step size and a -31°C PMT	63
29. Cathodoluminescence spectrum of amorphous Mn doped $\text{Li}_2\text{B}_4\text{O}_7$ at 10 KeV, 50 uA of current, 300/ 400/500 um slit width, 1 Å step size and a -31°C PMT	64
30. Cathodoluminescence spectrum of amorphous Mn doped $\text{Li}_2\text{B}_4\text{O}_7$ at 5 KeV, 50 uA of current, 500 um slit width, 1 Å step size and a -31°C PMT	64

Figure	Page
31. Cathodoluminescence spectrum of amorphous Mn doped $\text{Li}_2\text{B}_4\text{O}_7$ at 5,4,3,2, and 1.5 KeV, 50 uA of current, 1mm slit width, .1 integration time, and a -31°C PMT	65
32. Four peak Gaussian fit for the 5 KeV spectra at 2.710, 3.035, 3.513, and 3.932 eV for amorphous Mn doped $\text{Li}_2\text{B}_4\text{O}_7$ 50 uA of current, 1mm slit width, .1 integration time, and a -31°C PMT.....	66
33. TGM photoemission spectra of tantalum wire and Mn Doped $\text{Li}_2\text{B}_4\text{O}_7$ with 95 eV photons at room temperature.....	67
34. Photoemission spectra of undoped $\text{Li}_2\text{B}_4\text{O}_7$ with a TGM and 95 eV photons at 400 °C [4]	68
35. Binding energy versus intensity for Mn doped $\text{Li}_2\text{B}_4\text{O}_7$ with 110 eV photons at various temperatures.....	69
36. Binding energy versus intensity for Mn doped $\text{Li}_2\text{B}_4\text{O}_7$ with 110 eV photons at various temperatures after second sputter and annealing.....	71
37. NIM Photoemission spectra at 27 eV at various temperatures	73
38. E_{fermi} , E_v , and surface states for Mn doped $\text{Li}_2\text{B}_4\text{O}_7$	74
39. NIM PES of Mn doped $\text{Li}_2\text{B}_4\text{O}_7$ at 200°C and photon energies ranging from 24-32 eV.....	75
40. NIM PES spectra with 26 eV photon energy at 20 meV step size.	76
41. Temperature Dependent NIM PES Spectra with 26 eV photon energy.	76

List of Tables

Table	Page
1. Measured and Standard Wavelengths for the non VUV system.....	53
2. Mean Gaussian energies for luminescence spectra in Figure 24.	59

CATHODOLUMINESCENCE AND PHOTOEMISSION OF UNDOPED AND MN DOPED LITHIUM TETRABORATE

Introduction

Overview

In order to better protect the United States against further acts of terrorism within its borders, ports of embarkation, and abroad, smaller, more reliable, sensitive and faster special nuclear material detection capabilities must be explored. Neutron detection has the advantages of low natural background count, few neutron sources in normal commerce operations, and different shielding characteristics compared to gamma rays. Current neutron detection devices are, however, not sensitive enough, bulky, and too expensive for wide use applications. [1] The ideal neutron detector would either be hand held or small enough to be used at ports of embarkation or attached to cargo entering the United States.

Background

A primary advantage of using solid state media such as semiconductors for detectors is that more dense material yields smaller devices. Current technology provides a thin-film neutron detector consisting of a semiconductor diode requiring a layer of a neutron absorbing material and a moderator to capture neutrons or a conversion layer device. The challenge of the conversion layer device is the required thickness of the conversion layer. Current conversion

layers consist of 30 to 40 μm of enriched ^{10}B . If the conversion layer is too thin neutrons are not captured completely. Likewise, if the conversion layer is too thick, the daughter fragments will not reach the semiconductor. Conversion layers decrease the efficiency of solid state devices even with optimal thicknesses. [2]

Solid state neutron device design must utilize a material with a high neutron absorption cross section. Lithium tetraborate, $\text{Li}_2\text{B}_4\text{O}_7$, is a crystalline material containing high densities of ^6Li and ^{10}B , both materials with high neutron absorption cross sections. The ^{10}B neutron capture cross section for thermal neutrons is 3850 barns and ^6Li has a cross section of 940 barns. [3] There are three design proposals utilizing lithium tetraborate as a neutron detector. The first involves either a heterogeneous PN or PIN semiconductor with a Gd-doped semiconductor and $\text{Li}_2\text{B}_4\text{O}_7$. Such a design would allow for the Gd-doped side to detect fast neutrons while the $\text{Li}_2\text{B}_4\text{O}_7$ would detect slow neutrons. A second design would be a homojunction PN or PIN semiconductor with doped $\text{Li}_2\text{B}_4\text{O}_7$. Finally, in a third design, $\text{Li}_2\text{B}_4\text{O}_7$ could be utilized as a conversion layer for a traditional semiconductor. [2] As a borate, $\text{Li}_2\text{B}_4\text{O}_7$ will be compatible at the interface with any Gd oxide due to oxide-oxide interface potential. In addition, $\text{Li}_2\text{B}_4\text{O}_7$ will be chemically stable with other rare earth oxides which is a necessity for device fabrication. [4]

Since neutrons are neutral they must be detected through nuclear reactions creating charged particles which are detected by radiation detectors. $\text{Li}_2\text{B}_4\text{O}_7$ would be utilized in slow neutron detection. Slow neutrons, neutrons less than 0.5 eV, are detected by nuclear conversion reactions such as (n,α) or (n,p) reactions. In such a neutron detector, the neutron generates fast charged particles and the fast charged particles lose their energy generating electron hole pairs.

The intensity with respect to time is then proportional to the incident neutron flux. The common detector conversion reactions are:

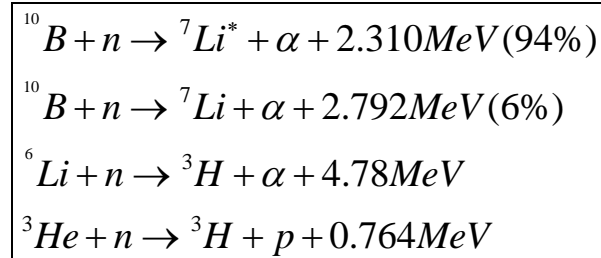


Figure 1. Detector Conversion Reactions [5]

Research Focus

The primary objective of this research is to determine the material characteristics of doped $\text{Li}_2\text{B}_4\text{O}_7$ in order to produce more efficient neutron detection devices. Since $\text{Li}_2\text{B}_4\text{O}_7$ is an insulator, it is necessary to dope it with impurities such as manganese, copper, or silver so it may become p type, and thus increase the number of positive charge carriers, or n type to increase the number of electron charge carriers. This would allow for the use of $\text{Li}_2\text{B}_4\text{O}_7$ in heterojunction or homojunction semiconductor devices. An accurate bandmap and electronic configuration of undoped $\text{Li}_2\text{B}_4\text{O}_7$ exists. [6] Through a combination of cathodoluminescence and photoemission spectroscopy the doped $\text{Li}_2\text{B}_4\text{O}_7$ electronic band structure and other surface and bulk characteristics can be determined.

$\text{Li}_2\text{B}_4\text{O}_7$ Structure

$\text{Li}_2\text{B}_4\text{O}_7$ is a tetragonal crystal with a space group I4cd with 104 atoms per unit cell. It has a density of 2.44 g/cm^3 and is a strong insulator with a band gap of approximately 9-10 eV. [4] The lattice parameters characterizing the $\text{Li}_2\text{B}_4\text{O}_7$ unit cell are $a=9.477 \text{ \AA}$ and $c=10.286 \text{ \AA}$

The crystal motif of $\text{Li}_2\text{B}_4\text{O}_7$ is the boron-oxygen compound (B_4O_9). [6] There are two planar trigonal BO_3 and two tetrahedral BO_4 motifs with lithium atoms at the interstices along the z axis. One of the eight unit cells of a molecule of $\text{Li}_2\text{B}_4\text{O}_7$ is seen below. [4]

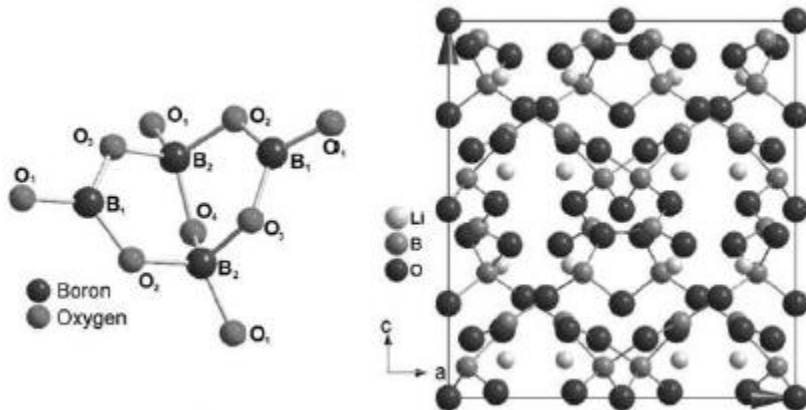


Figure 2. Basic $[\text{B}_4\text{O}_9]^{-4}$ structural unit of $\text{Li}_2\text{B}_4\text{O}_7$ (left); orientation of B_4O_9 structural units and Li^+ ions in the crystal lattice (right) [7]

Thus, $\text{Li}_2\text{B}_4\text{O}_7$ is a rigid anion sublattice formed from a boron-oxygen three dimensional network where the basic structure is the $[\text{B}_4\text{O}_9]^{-9}$ group with two boron atoms in triangular coordination and the other two boron atoms in tetrahedral coordination. These groups are combined with the common oxygen atoms in a spiral axis of 4I symmetry. Within the anion sublattice there are channels oriented along the direction [001] where the four lithium atoms are weakly bound to the anion sublattice. The boron-oxygen tetrahedra bonds are formed from the attachment of the oxygen atoms at the intersection of Li_2O and B_2O_3 . The lithium cations are near the $[\text{BO}_4]$ tetrahedra which compensates the excess negative charge. Therefore if the lithium cation is separated from the $[\text{BO}_4]$ tetrahedra, it becomes a negative point defect. One possibility for the negative point defect is to become a hole trap. An oxygen vacancy produces positive charge defects, or holes, which can trap electrons. [7] $\text{Li}_2\text{B}_4\text{O}_7$'s valence electrons of

interest are one in the $2s^1$, three in $2s^22p^1$, and six in the $2s^22p^4$ for Li, B and O, respectively.

These electrons in the s and p atomic orbitals create orbital hybridization and molecular bonds.

[4]

The $\text{Li}_2\text{B}_4\text{O}_7$ was grown by the Czochralski process. High purity $\text{Li}_2\text{B}_4\text{O}_7$ was grown from a stoichiometric melt using platinum crucibles. Synthesis of $\text{Li}_2\text{B}_4\text{O}_7$ included ${}^6\text{Li}_2\text{CO}_3$ with 96% ${}^7\text{Li}$ isotope, H_3 with ${}^{10}\text{BO}_3$ with 97.3% isotope, and H_3 ${}^{11}\text{BO}_3$ with 99.2% ${}^{11}\text{B}$ isotope at 917°C . [8] Dehydrated high-purity B_2O_3 , Li_2CO_3 , and MnO_2 was used to prepare the Mn doped $\text{Li}_2\text{B}_4\text{O}_7$ in a platinum crucible in the ambient atmosphere. The mixture had up to 0.3% molality of B_2O_3 in order to compensate for the evaporation losses of $\text{Li}_2\text{B}_4\text{O}_7$ [18]. A solid seed crystal was rotated and slowly extracted from a molten Mn doped $\text{Li}_2\text{B}_4\text{O}_7$. The seed crystal is then pulled upward and rotated simultaneously producing a large cylindrical shaped Mn doped $\text{Li}_2\text{B}_4\text{O}_7$ crystal.

$\text{Li}_2\text{B}_4\text{O}_7$ is a strong insulator, which is problematic in a cathodoluminescent study due to the fact that the surface charges up when electron energies of from 2-10 keV are applied. The electrons of $\text{Li}_2\text{B}_4\text{O}_7$ are tightly bound and not free to move around. Once the surface is charged, however, patches of immobile electrons remain on the surface. At electron beam energies above 2 keV, the surface becomes increasingly negative. At electron energies below 1.5 eV this charging begins to decrease. However, at such low energies, the cathodoluminescent signal is weak which results in a very small signal to noise ratio. Measurements using high and low electron gun energies were used in this current study to investigate this dependence of cathodoluminescence on charging. Note that with lower voltages, the concentration of excitation

energy is in a smaller volume of the sample since the electron range shrinks at low beam energies. This concentration of power might give rise to Coulomb aging. Since surface charging creates non-radiative pathways for energy loss, a sizable decrease in cathodoluminescence efficiency occurs. [9]

Theory

Band Gap Theory

According to band theory there are three primary classifications for crystalline materials; conductors, insulators, and semiconductors. The classification of a material as a conductor, insulator, or semiconductor, is dependent on the available electron energies. These electron energy states form bands of states. The conduction process is dependent on whether the electrons are in the valence or conduction bands of the energy diagram. Insulators have a large energy gap from the conduction to the valence band requiring a significant amount of energy to overcome. Metals, or conductors, have valence bands overlapping the conduction band. Semiconductors have a small energy gap between the conduction and valence band. Electrons can be excited thermally, optically, or radioactively across the semiconductor energy band gap. At 0 K all electrons in a semiconductor or insulator are located in the valence band. As the temperature increases, the electrons may be easily excited into the conduction band. The addition of a small percentage of foreign or impurity atoms in the crystal adds energy states in the energy bandgap which can increase the conductivity significantly. This process is called doping. Figure 3 shows the energy band diagrams for insulators, semiconductors, and metals.

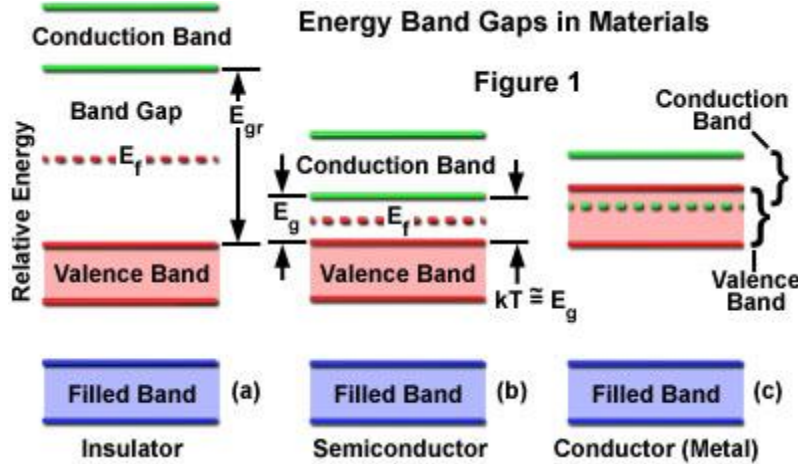


Figure 3. Energy Level Diagrams for Insulators, Semiconductors, and Metals [10]

Small amounts of impurities are found in all crystals. Some semiconductors or insulators are intrinsic and others extrinsic where dopants have been added, to produce a desired effect.

$\text{Li}_2\text{B}_4\text{O}_7$ was doped with Mn to produce either an n-type (donor) or p-type (acceptor) semiconductor. An n-type crystal occurs when an impurity donates weakly bound electrons to the conduction band creating excess negative charge carriers. P-type crystals occur when an impurity produces a hole creating excess positive charge carriers. The holes are in states near the valence band allowing for electrons in the valence band to ionize these acceptor states. Both electrons and holes can move throughout the conduction band of $\text{Li}_2\text{B}_4\text{O}_7$ producing a current.

Cathodoluminescence Synopsis

Cathodoluminescence (CL), is the emission of photons from a solid material, such as a semiconductor, when the material is excited by an incident beam of energetic electrons or cathode rays. If the photons are emitted from a direct transition from the conduction to valence band within about 10^{-8} seconds, the luminescence is referred to as fluorescence.

Phosphorescence is luminescence occurring after the excitation from the electron source has ended. Luminescence in semiconductors is explained by the radiative recombination of electron-hole pairs. Transitions in semiconductors may occur from the conduction to valence band or from impurity levels in the band gap due to donors and acceptors. [11]

Cathodoluminescence is a process in which valence electrons are excited by a beam of electrons from an electron gun, and undergo transitions from the valence to the conduction band. The empty state left in the valence band is described as a hole. The electrons then recombine with the holes in the valence band via several different radiative or non-radiative transitions.

Intraband transitions occur when an electron, excited far above the conduction band, trickles down to the bottom of the conduction band, finally reaching thermal equilibrium with the lattice. This process can result in phonon emission. (Figure 4-1) Interband transitions are direct recombinations of the electron in the conduction band with the hole in the valence band. The result is a photon with a broad emission spectrum due to transitions from states at or near the corresponding band edges. (Figure 4-2) [11]

A third transition mechanism involves excitons. Excitons are two particle systems similar to a hydrogen atom. An electron in the conduction band orbits a hole in the valence band forming a bound electron-hole pair which is free to move around the lattice. This is a free exciton. With excitonic recombination, the electron and hole recombine conserving momentum during the transition. (Figure 4-3) The energy of light emitted is less than the bandgap energy by the binding energy of the exciton. The excitonic energy, E_x , which is material dependent, is:

$$E_x = \frac{m_r^* q^4}{2h^2 \varepsilon^2 n^2} \quad (1)$$

where m_r^* is the reduced mass, q is the charge of an electron, h is Planck's constant, ε is permittivity, and n is the quantum number. Excitonic emissions are usually observable only at low temperatures. [12]

There are also excitons, called bound excitons, in which the electron-hole pair is bound to an impurity. Either the hole or the electron is trapped at an impurity atom and the other orbits. The energy of the emitted light is less the exciton energy and the energy of the impurity. Therefore, different impurities create different bound exciton peaks.

Electrons may also undergo a transition from the conduction band to the valence band through donor and acceptor levels in the energy gap producing extrinsic luminescence. Transitions from the donor state to the valence band or from the conduction band to an acceptor state produce extrinsic luminescence. (Figure 4-4, 5) Finally there is a donor acceptor transition or donor-acceptor pair (DAP) recombination. (Figure 4-6) In a semiconductor, the carriers can be trapped at the donor or acceptor sites to produce neutral donors and acceptors. When returning to equilibrium some of the electrons on donor sites will recombine with holes on the neutral acceptors producing extrinsic luminescence. There is columbic interaction between the ionized donors and acceptors. The energy of the photons emitted in this donor-acceptor transition is:

$$\hbar\omega = E_g - E_A - E_D + \frac{q^2}{\varepsilon r} - \frac{q^2 b^5}{\varepsilon r^6} \quad (2)$$

where $E_{g,A,D}$ are the energies of the gap, acceptors, and donors respectively, r is the distance between the donor and acceptor, b is an adjustable van der Waals parameter and ϵ is the static dielectric constant. The coulomb interaction between the donor acceptor pairs separated by r is $\frac{q^2}{\epsilon r}$, and $\frac{q^2 b^5}{\epsilon r^6}$ is the polarization term only applicable to very close pairs. When r is large the discrete lines will form a continuum and broad DAP bands are observed. [12] In DAP and excitonic absorption, the external photon creates a pair of positive and negative charges, lowering the energy required to excite the charges. At high excitation energies in DAP recombination emission a sharp pair of lines are observed; with low excitation energies, distant-pair transitions are dominant. Hence the radiative transition probability is

$$P(r) = P_0 e^{(\frac{-2r}{a})} \quad (3)$$

where a is the Bohr radius of the less tightly bound pair and P_0 is constant and is the limiting transition probability as $r \rightarrow 0$. Therefore the recombination rate depends on the radius. [11] Excitation and radiative deexcitation of an impurity within incomplete inner shells is shown in Figure 4-7.

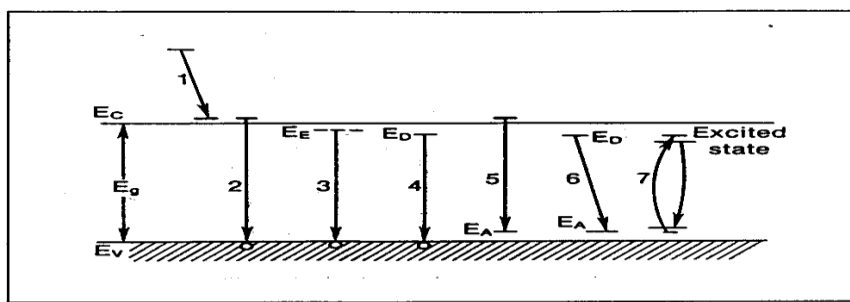


Figure 4. Schematic diagrams of radiative transitions between the conduction band (E_c), the valence band (E_v) and the exciton (EE), donor (Ed) and acceptor levels (EA) in a semiconductor. [11]

Transitions between deep donors and deep acceptors will have recombination emission with lower photon energies than the band gap. Shallow donor or acceptors will have transition energies near the energy of the band gap. Therefore to distinguish between band to band transitions from shallow donor and acceptors, the sample must be cooled to liquid helium temperatures to reduce thermal broadening, reducing acoustic phonon interference and hence increase the signal to noise ratio. [11]

Cathodoluminescence analysis, when performed in vacuum, is a beneficial tool to provide material characterization. It is a nondestructive method that can be used to analyze a material at different depths, depending on the electron's beam energy used. Typically, beam energies of 500 eV to 10 keV are used to probe the surface from several nanometers to several hundred nanometers below the surface. Since $\text{Li}_2\text{B}_4\text{O}_7$ is determined to be a material with a bandgap of approximately 9 - 10 eV, the electron beam excitation will result in recombination photons at wavelengths as short as 1200 Å, the so-called vacuum ultraviolet portion of the optical spectrum. Analysis of such vacuum ultraviolet radiation requires an evacuated spectrometer and beam path since radiation of wavelengths less than approximately 1800 Å are absorbed by the atmosphere. As a result such a cathodoluminescence experiment must be conducted in a vacuum environment.

Electron Energy Disposition.

When a solid is excited by an electron beam's energetic electrons, the incident electrons are either absorbed or scattered by the atoms in the surface of the solid. This excitation results in the production of electron-hole pairs which recombine resulting in light emission. Since the

excited state's lifetime is relatively short a photon is emitted, hence resulting in luminescence. This luminescence is due to an electronic transition between an initial state, E_i , and the final state, E_f . The energy or wavelength is given by:

$$E_f - E_i = \frac{hc}{\lambda} = h\nu. \quad (4)$$

That is, the photon wavelength (in microns) is related to photon energy E (in eV) by $\lambda = \frac{hc}{E}$.

[11] In the case of $\text{Li}_2\text{B}_4\text{O}_7$ wide band gap materials, this emission of photons occurs from the visible to the far ultraviolet, i.e., from approximately 2 to 9 or 10 eV. Many emissions are at longer wavelengths such as the near infrared region. As an electron beam interacts with a solid the electron's energy is dissipated. It is important for cathodoluminescence analysis to understand the generation of carriers in the solid.

For electron energies from 20 to 50 keV and solids of low to intermediate atomic number, elastic scattering of the electrons can be analyzed using the Rutherford scattering cross section, σ , which is given by

$$\sigma = (5.21 * 10^{-21}) \left(\frac{Z}{E} \right)^2 \frac{4\pi}{\delta(\delta+1)} \left(\frac{E + m_0 c^2}{E + 2m_0 c^2} \right) \quad (5)$$

where Z is the atomic number of the scattering atom, E is the electron energy in KeV, m_0 is the rest mass of the electron, c is the speed of light, and δ is a screening parameter

$$\delta = (3.4 * 10^{-3}) \frac{Z^{0.67}}{E}. \quad (6)$$

The scattering angle, θ , can be determined from the probability of elastic scattering into a particular range (0 to θ) and hence the probability distribution is:

$$\cos(\theta) = 1 - \frac{2\delta R}{1 + \delta - R} \quad (7)$$

and R is a randomly distributed number from 0 to 1. If electron energies are less than 50 keV the relativistic correction is ignored. [11]

For electron energies less than 20 keV or for heavier elements, there is a large deviation from the Rutherford method, therefore

$$\sigma_R(\theta) = \frac{e^4 Z^2}{16(4\pi\epsilon_0 E)^2} \frac{d\Omega}{\left[\sin^2\left(\frac{\theta}{2}\right) + \left(\frac{\theta_0^2}{4}\right) \right]^2}. \quad (8)$$

$\left(\frac{\theta_0^2}{4}\right)$ is the screening parameter defined by $3.4 \times 10^{-3} Z^{2/3}/E$, θ is the scattering angle from 0 to π ,

and ϵ_0 is the dielectric constant.

Bethe's expression is best suited for high atomic number solids and low electron energies. The mean rate of energy loss for distance, S , traveled in a solid is used to determine inelastic scattering according to Bethe is

$$\frac{dE}{dS} = -2\pi q^4 N_A \frac{\rho Z}{EA} \ln\left(\frac{1.166E}{J}\right). \quad (9)$$

The charge of the electron is q , Avogadro's number is N_A , density is ρ , the atomic weight is A , E is the mean electron energy, and J is the mean ionization potential. J in keV is given by

$$J = (9.76Z + 58.5Z^{-19})10^{-3}. \quad [11] \quad (10)$$

Incident electrons undergo successive inelastic and elastic scatters. Elastic scattering of electrons causes the original trajectories in the material to be randomized. The total length of the electron's random walk is the Bethe range which is calculated from equations (9) and (10). The Gruen range of electron penetration is a function of electron beam energy E_b ,

$$R_e = (k / \rho)E_b^\alpha \quad (11)$$

where k is a function of energy dependent on the atomic number. The constant α , which can be determined from published charts, also depends on the atomic number and on E_b , the electron beam energy in keV. The effective depth to which the electrons dissipate their energy is called the Gruen electron beam penetration range. The excitation volume or generation volume R_e , in μm , can be calculated from the Kanaya and Okayama model as

$$R_e = (0.0398 / \rho)E_b^{1.75}(\mu\text{m}). \quad [11] \quad (12)$$

The excitation range according to Kanaya and Okayama is

$$R_e = (0.0276A / \rho Z^{0.889})E_b^{1.67}(\mu\text{m}). \quad [11] \quad (13)$$

The shape of the excited volume of material is dependent on the atomic number. For low Z the volume analyzed is pear shaped, spherical for Z between 15 and 40, and hemispherical for larger atomic numbers. With CL one electron can create thousands of electron hole pairs the

volume of which is normally several microns in diameter. The number of electron hole pairs generated is the generation factor, G and is defined as

$$G = E_b(1-\gamma)/E_i. \quad (14)$$

E_b is the electron beam energy, E_i is the ionization energy, and γ is the fractional electron beam energy loss from backscattered electrons. E_i is related to the band gap energy by $E_i = 2.8E_g + M$. M is electron beam independent but material dependent and ranges from 0 to 1 eV. The local carrier generation rate is

$$g(r, z) = \frac{\langle g \rangle GI_b}{q} \quad (15)$$

where $\langle g \rangle$ is the ionization energy normalized distribution in the generation volume, I_b is the current of the electron beam, and q is the elementary charge. [11]

Using the Monte Carlo electron trajectory calculations, electrons elastic and inelastically scatter and are backscattered out of the target. The electron path is calculated in a stepwise manner. Each electron travels a small straight line distance between random scattering and the scattering angle is selected randomly by R . If the angle scattering is from elastic collisions, the energy loss is continuous and

$$S = -\lambda \ln(|R|) \quad (16)$$

where λ is the mean free path from the total scatter cross section,

$$\lambda = \frac{A}{N_A \rho \sigma}. \quad (17)$$

Energy loss is calculated from dE / dS until it is lower than the electron's ionization energy.

With the Monte Carlo method, backscatter, γ , can also be calculated by dividing the number of backscattered electrons by the total number of trajectories. The Monte Carlo method must be calculated for at least 1000 trajectories and the resulting boundaries of the generic volume are not well defined. The Monte Carlo method confirms a substantial fraction of energy dissipated occurs in a small volume where the electron beam impacts the surface. [11]

Cathodoluminescence Signal.

The spontaneous emission rate between two energy levels is determined by the Einstein coefficient, A . If the upper level has a population N at time t , the recombination rate is

$$\left(\frac{dN}{dt} \right) = -AN$$

or

$$N(t) = N_0 e^{-At} = N_0 e^{\frac{-t}{\tau_R}}$$
(18)

where τ_R is the radiative lifetime of the transition, A^{-1} . The luminescence intensity at a frequency, ν , is

$$I(h\nu) \propto |M|^2 g(h\nu)^* (\text{level occupancy factors}). [13] \quad (19)$$

The level occupancy factors includes the probability the relevant upper level is occupied and the lower level is empty. M is the transition matrix element, and $g(h\nu)$ is the transition density of states. The quantum mechanical transition probability is given by Fermi's golden rule. Lattice vibrations and traps can generate relaxation paths and the luminescence efficiency, η_R , is

$$\frac{dN}{dt}_{total} = -\frac{N}{\tau_R} - \frac{N}{\tau_{RN}} = -N \left(\frac{1}{\tau_R} + \frac{1}{\tau_{RN}} \right) \quad (20)$$

τ_R and τ_{RN} are the radiative and non-radiative recombination rates. Therefore η_R is

$$\eta_R = \frac{AN}{N \left(\frac{1}{\tau_R} + \frac{1}{\tau_{RN}} \right)} = \frac{A}{\left(1 + \frac{\tau_R}{\tau_{RN}} \right)} \quad (21)$$

where $A = \tau_R^{-1}$. When $\tau_{RN} \ll \tau_R$, η_R approaches unity, the light emission is efficient. [13]

Photoemission Spectroscopy

In photoemission spectroscopy, photons from a light source impact a solid. Electrons in the surface of the solid are excited and then escape into the vacuum where they are analyzed with respect to their kinetic energy, E_{kin} , and momentum with an electrostatic analyzer. Figure 5 depicts the photon striking the surface of the sample where, through the photoelectric effect, photoelectrons are emitted into the vacuum where they are measured using the energy analyzer and electron detector.

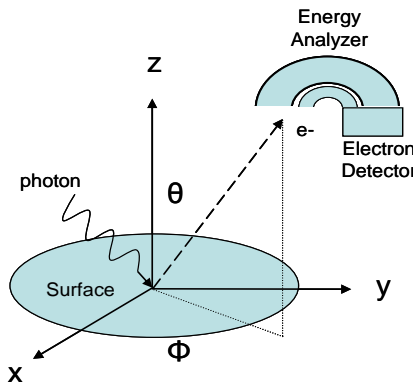


Figure 5. Diagram of photoemission spectroscopy

The primary quantity measured in photoemission spectroscopy is the E_{kin} of the emitted photon, the electron's angle with respect to the initial photon light source, and the electron's angle to the surface. Binding energy is determined from the energy of the initial incident photons from the light source and the work function of the material.

$$E_{kin} = \hbar\omega - \phi - |E_b| \quad (22)$$

where E_b is the binding energy, ϕ , is the work function, and $\hbar\omega$ is the energy of the incident light. [14] Therefore momentum, p , is

$$p = \sqrt{2m_e E_{kin}} \quad (23)$$

where m_e is the mass of the electron.

Figure 6 depicts the association between a metal energy level diagram and photoemission spectra. The valence band electrons are emitted from the sample first with the highest kinetic energy, i.e. the energy of the incident photon minus the work function of the material, ϕ . More of the photon's energy is utilized in probing the energy bands associated with the core level electrons causing their emission to be at lower kinetic energies. The Fermi level energy is the guideline for understanding the photoemission energy distribution. Determination of the Fermi level for this system is based on the fact that the Fermi level of the Mn doped $\text{Li}_2\text{B}_4\text{O}_7$ and that of the metal sample holder must be the same.

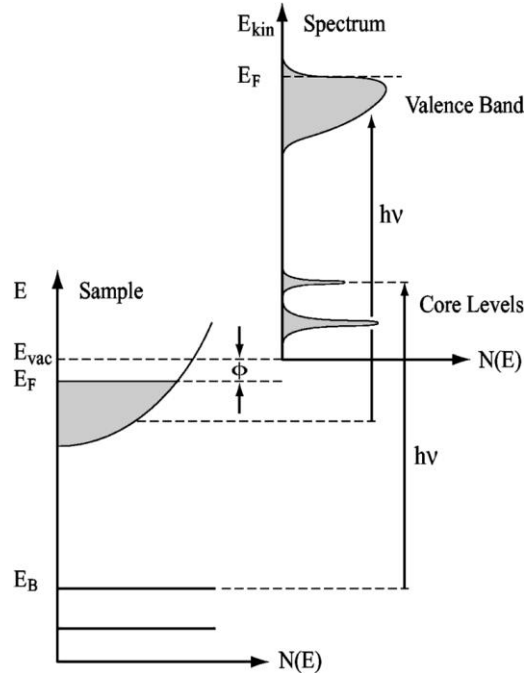


Figure 6. Photoemission energy level diagram and spectrum

The photothreshold energy, I , is defined as the energy required to leave the solid or the summation of binding energy and the work function. If the photon energy, $\hbar\omega$, is equal or less than I , then no photoelectrons escape the vacuum. Photoelectrons from the valence band produce I equal to the energy difference from the top of the valence band to the vacuum level less the work function energy. The electron affinity is the energy difference from the conduction band to the vacuum level. The photothreshold energy, work function, and electron affinity are defined as

$$\begin{aligned} I &= \hbar\omega - e(V_v - V_o) \\ \phi &= \hbar\omega - e(V_F - V_o) \\ \chi &= I - E_g \end{aligned} \tag{24}$$

where V_0 is the potential where photoemission disappears, V_V is the potential at the top of the valence band, V_F is potential of the Fermi Level, and E_g is the band gap energy.

Since the electron's mean free path is approximately a few Å for electron energies from 10 to 2000 eV, only the electrons in a very thin layer on the surface of the sample are available for photoemission.

Photoemission spectroscopy was utilized to understand electron structure and the bandgap of Mn doped $\text{Li}_2\text{B}_4\text{O}_7$. Two types of photoemission systems were used; one using a NIM, or normal incident monochromator, and one using a TGM, or toroidal grating monochromator. Both systems provide a tunable photon source for energy dependence and bulk measurements, a plane-polarized light source for characterizing the type of molecular orbitals present, and a very high brightness source. Both of these systems, which utilize the synchrotron ring at the Center for Advanced Microstructures and Devices (CAMD) of the Louisiana State University in Baton Rouge, LA, will be discussed in the methodology section.

Surface States.

Surface states are formed at atomic layers close to the surface and change the electronic band structure of the bulk material at the vacuum-solid interface where new electronic states or surface states are formed. Tamm demonstrated that a periodic square well potential, based on the Kronig-Penney crystal model, terminated on one side by a surface potential barrier, provided additional allowed discrete levels within the forbidden energy region near the bulk band edge. The additional levels correspond to wave functions localized near the surface for each atom. There is one surface state for each surface atom and localized surface levels which arise from

impurity atoms or oxide layers and structural imperfections at the surface. [15] This model is valid for tight binding states or d and f valence band transitions. Surface states split off from the unperturbed band and are often called Tamm states. At the surface the d and f states experience a weaker crystal potential than in the bulk resulting in a split off state. [14]

In an infinite crystal the propagating electronic states have real wave vectors. States with energies in the forbidden energy gap are not allowed. Electron states in the gap arise from a complex wave vector, $k=p+iq$ with exponential wave functions that have real exponents $e^{(+-qz)}$ for a one dimensional crystal in the $+-z$ direction. Since these states diverge as z approaches positive or negative infinity, they are forbidden in the infinite crystal. With a semi-infinite crystal there are exponentially decaying eigenfunctions outside the crystal and wave functions inside the crystal leading to surface states. These states are viewed by Echenique and Pendry as electrons trapped between the surface of the crystal via a band gap and the surface barrier potential, preventing them from leaving the crystal and escaping into the vacuum. [14]

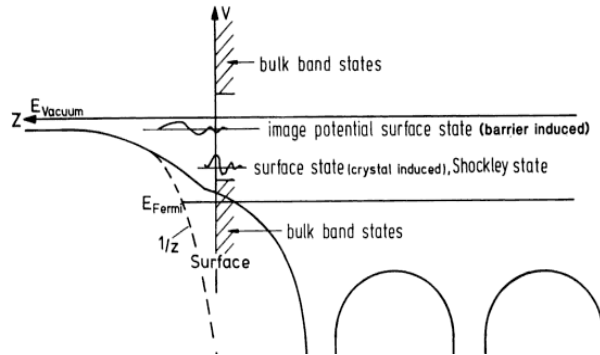


Figure 7. Echenique and Pendry view of surface states. The electron is trapped between the crystal surface and the image potential traveling back and forth between the two barriers.

The above figure is the barrier image potential for the Echenique and Pendry view of surface states. The electron is trapped between the crystal's surface and the image potential. The energy of the trapped electrons is calculated from

$$E_{vac} - E_m = \frac{0.85}{m^2}$$

where $m = 1, 2, \dots$, E_{vac} is the vacuum energy and E is the energy of the bound states.

Covalently bonded crystals and crystals with localized and highly anisotropic d-orbitals contribute to bonding, electron states on the surface, and dangling bond states. Dangling bond states are created by cutting the bonds between atoms with partially filled orbitals outside the crystal's surface. These bonds are aggressive in nature, they saturate by binding atoms and molecules in an infinite vacuum decreasing the intensity of surface state features over time.

Ionic insulator surfaces are usually not perfect. Defects and vacancies are common and make it difficult to prepare a stoichiometric surface. Localized electronic states are associated with defects. Each crystal's surface properties are dependent on the density of these surface levels and their energy distribution. A considerable density of surface states creates a surface depletion layer or accumulation layer. The surface will be filled to E_{fermi} producing a layer of negative charge at the surface repelling electrons in the conduction band away from the surface. This creates a positive surface space charge layer from the uncompensated donor ions. A depletion region and surface potential barrier are established by the equilibrium between the bulk insulator and the surface states independent of any external contact. Since the crystal is electrically neutral, the total charge in the space charge region of the crystal is equal in

magnitude to the charge of the surface state electrons, creating a surface potential, ϕ_s adjacent to the surface. [15] Thus, surface states are important in the interpretation of both photoemission as well as cathodoluminescence data from materials such as Mn doped $\text{Li}_2\text{B}_4\text{O}_7$.

Literature Review

History

At the outset, Mn doped $\text{Li}_2\text{B}_4\text{O}_7$ has been studied for applications in medical therapy dosimetry. Since $\text{Li}_2\text{B}_4\text{O}_7$'s Z_{eff} , the effective nuclear charge, is smaller than that of tissue cells it allows for a tissue-equivalent $\text{Li}_2\text{B}_4\text{O}_7$ phosphor if doped. In 1967 it was determined by Schulman, Kirk, and West that $\text{Li}_2\text{B}_4\text{O}_7$ has a single glow peak with good trap stability and a low residual dose. Also, $\text{Li}_2\text{B}_4\text{O}_7$ does not require any pre-irradiation annealing, and has high radiation-optical hardness, a wide transmission band, and mechanical strength. The thermal luminescence of Mn and Cu doped $\text{Li}_2\text{B}_4\text{O}_7$ did not match spectral sensitivities of commercial photomultipliers and was not sensitive to background radiation. Unfortunately, Mn doped $\text{Li}_2\text{B}_4\text{O}_7$ was supralinear over 100 rads and could not be utilized for dosimetry despite its ideal energy characteristics. [13]

Overview

In the late 1990's and early 2000's several papers were published on luminescence spectra of $\text{Li}_2\text{B}_4\text{O}_7$ due to an increased interest in electronic excitations and energy dissipation in radiation resistant nonlinear optical crystals. These papers provided the initial scientific experiments carried out on $\text{Li}_2\text{B}_4\text{O}_7$. Although the study of $\text{Li}_2\text{B}_4\text{O}_7$ has been underway in certain areas for some time, at present there are very few cathodoluminescence studies of

undoped $\text{Li}_2\text{B}_4\text{O}_7$ and research on cathodoluminescence and photoemission of Mn doped $\text{Li}_2\text{B}_4\text{O}_7$ is nearly nonexistent.

The underlying expansion of research in Mn doped $\text{Li}_2\text{B}_4\text{O}_7$ is due to a desire to understand the physical location of dopants and their energy levels in order to determine the suitability of $\text{Li}_2\text{B}_4\text{O}_7$ as a neutron detecting semiconductor. This section will present a brief review of what is already published regarding both $\text{Li}_2\text{B}_4\text{O}_7$ and Mn doped $\text{Li}_2\text{B}_4\text{O}_7$ and how the present cathodoluminescence and photoemission research will provide a more in-depth understanding of Mn doped $\text{Li}_2\text{B}_4\text{O}_7$.

Background Research on $\text{Li}_2\text{B}_4\text{O}_7$

The electronic structure of $\text{Li}_2\text{B}_4\text{O}_7$ crystals was studied using cluster calculations and x-ray photoelectron spectroscopy. It was determined that the valence band states of $\text{Li}_2\text{B}_4\text{O}_7$ are 2-15 eV below the Fermi level. These valence band state are comprised of the boron-oxygen group $[\text{B}_4\text{O}_9]^{6-}$ since lithium stabilizes the crystal and is minimally involved in the valence band formation. The oxygen atoms O(2) and O(3) in $[\text{B}_4\text{O}_9]^{6-}$ join each B(1) triangle with two B(2) tetrahedral, both having an O(4) in common. X-ray photoelectron spectroscopy of $\text{Li}_2\text{B}_4\text{O}_7$ identified three peaks below E_f . A peak near 25 eV represents the O 2s quasicore states. Binding energies of the core levels for Li 1s, B 1s, and O 1s were determined to be 55.7, 192.4, and 531.8 eV respectively.[17]

In order to improve solid-state laser technology, transient optical absorption and luminescence in $\text{Li}_2\text{B}_4\text{O}_7$ was studied in the visible and UV spectral regions using absorption

optical spectroscopy with nanosecond time resolution. In $\text{Li}_2\text{B}_4\text{O}_7$, the optical transition originated from hole centers. Relaxation occurred due to inter-defect tunneling recombinations involving hole centers and electronic Li^0 centers. At 290 K, the lithium center migrated one dimensionally without ejecting carriers into the conduction or valence bands. Using pulsed cathodoluminescence, it was determined that the relaxation process is connected to an electron tunneling from a deep center to a small polaron hole migrating close by.[18]

According to the transient absorption data, $\text{Li}_2\text{B}_4\text{O}_7$ color centers are formed from native lattice defects resulting in absorption from 2-5 eV. Defects involving an interstitial lithium ion and a lithium vacancy are most likely to occur because the lithium atoms have a strong anharmonicity to the boron-oxygen framework. A hole O^- color center results in optical transitions from the top of the valence band into the band gap and finally to the O 2p states in the upper part of the valence band. The hole transfer among oxygen ions surrounding the defect decreases and can be ascribed to interpolaron absorption. When the hole is transferred from the ground state to the oxygen ions surrounding the lithium vacancy, optical absorption occurs. Tunneling recombination and a diffusion controlled reaction of annihilation between the lithium vacancies and interstitial occurs since at room temperature the lithium cations are mobile.[18]

The main pulsed cathodoluminescence band at 3.6 eV, according to Ogordnikov et. al., is from radiative annihilation of a self trapped exciton. Inter-defect tunneling recombination is a major part of the cathodoluminescence spectrum. A one-site small polaron acts as a short lived nucleus trapping holes, excitons, or electron-hole pairs. Electron tunneling transport from a deep electronic level to an excited level of a hole polaron moving near the trap center could create a

self trapped exciton in the σ state. Occurring 50% of the time, radiative annihilation of a self trapped exciton represents the σ polarized luminescence of $\text{Li}_2\text{B}_4\text{O}_7$. The annihilation is limited by tunneling recharging of the deep-electronic-center and hole polaron pair. $\text{Li}_2\text{B}_4\text{O}_7$ was also determined to have an F center due to the rapidly decaying band at 3.36 eV. These F centers were previously reported in LiB_3O_5 at 3.3 and 2.7 eV.[18]

In 2003, different dopants were added to $\text{Li}_2\text{B}_4\text{O}_7$ to create a laser host or gain medium. $\text{Li}_2\text{B}_4\text{O}_7$ doped with Yb, Co, and Mn ions were analyzed with thermoluminescence for nonlinear applications. The Mn^{2+} ion has transitions between energy levels within the $3d^5$ configuration and has a free ion ground state, 6S . The 6S is the only spin sextet state and an octahedral crystal field does not split it. Within an octahedral, a weak crystal field 6S transforms into $^6A_1(S)$ as the ground state. The absorptions are spin and parity forbidden within an octahedral environment. Therefore, absorption bands, especially for low concentrations of Mn, are very weak.[19] The optical transitions of a moderately doped crystal must be investigated by an excitation and emission technique such as cathodoluminescence.

Optical absorption, steady state, and time-resolved photoluminescence of single crystal and glassy Mn doped $\text{Li}_2\text{B}_4\text{O}_7$ were studied. In crystal form only Mn^{2+} ions are present, whereas in glassy Mn doped $\text{Li}_2\text{B}_4\text{O}_7$ had both Mn^{2+} and Mn^{3+} ions. The Mn ions are incorporated in different oxidation states such as Mn^{2+} ($3d^5$), Mn^{3+} ($3d^4$), Mn^{4+} ($3d^3$), and Mn^{5+} ($3d^2$). Each ion is luminescent and the photoluminescence pattern identifies them; however, some of the Mn ions present simultaneous emission spectra. The Mn ions produced excitation bands from 2000 to 5500 Å depending on the dopant concentration. With low dopant concentration, there was low

intensity of the parity and spin forbidden factor producing no optical absorption bands in the whole UV and visible region in the pure crystal. The glassy Mn doped $\text{Li}_2\text{B}_4\text{O}_7$ emitted a broad band from 4500 to 6000 Å. The Mn^{3+} ion are observed in optical absorption and excitation, while the Mn^{2+} ions are apparent in the emission spectrum.[20]

In another study, absorption bands in the Mn doped $\text{Li}_2\text{B}_4\text{O}_7$ were observed only under γ -ray irradiation. These transition peaks were observed at 2250, 3700, 4700, and 6100 Å. The 4700 Å is attributed to the Mn^{2+} absorption and the 6100 Å is attributed to the Mn^{5+} or F^{2+} color center absorption. The 2250 and 3700 Å peaks may be due to a F^+ color center, or a V_k center due to the lithium vacancy pair. The Mn^0B center replaced the lithium in an off-center position and the Mn^0 forms from Compton electron capture by the Mn^{1+} ion and the $\text{Mn}^{6+}(\text{d}1)$ ion. Finally there was a weak broad absorption band with a maximum at 8000 Å from the $\text{Mn}^{6+}(\text{T}_\text{d})^2\text{E}-^2\text{T}_2$ ligand-field transitions.[19] Therefore after γ -ray irradiation there were many radiation induced symmetries interacting with one another and different manganese ions present. Using low temperatures thermoluminescence, a spectrum produced five very narrow peaks demonstrating the piezoelectric quality of $\text{Li}_2\text{B}_4\text{O}_7$. Either electron or hole traps were found inside the bandgap of the crystal at 0.043 eV, 0.154 eV, 0.123 eV, and 0.240 eV. These are associated with F^+ or Mn^0B , V_k , Mn^{3+} , Mn^{6+} centers.

Afterwards, absorption data of $\text{Li}_2\text{B}_4\text{O}_7$ irradiated by thermal neutrons was measured to determine if this crystal was radiation hardened. Thermal neutrons with a fluence of 1.8×10^{16} cm^{-2} created defects due to the $^{10}\text{B}(\text{n},\alpha)^7\text{Li}$ reaction. These defects were dependent on the isotopic concentration of the $\text{Li}_2\text{B}_4\text{O}_7$. Induced absorption from 2800 to 2940 Å occurs in

${}^6\text{Li}_2{}^{10}\text{B}_4\text{O}_7$ and ${}^7\text{Li}_2{}^{10}\text{B}_4\text{O}_7$ crystals. The ${}^7\text{Li}_2{}^{10}\text{B}_4\text{O}_7$ crystals have an absorption band due to color centers that did not overlap with the luminescence from the crystal at 3650 Å. Since both ${}^6\text{Li}$ and ${}^7\text{Li}$ have the same absorption spectra, the crystal structures are not formed in the $\text{Li}_2\text{B}_4\text{O}_7$ lattice due to ${}^6\text{Li}^3(\text{n},\alpha){}^3\text{H}$. Fast neutrons produced radiation damage from knock-on damage for all isotopic concentrations. The primary radiation defects are crystal clusters of Li_2O .[9]

The affect of annealing on Mn doped $\text{Li}_2\text{B}_4\text{O}_7$ was analyzed using thermo-stimulated luminescence. The annealing of the Mn doped $\text{Li}_2\text{B}_4\text{O}_7$ resulted in a sharp intensity drop for both luminescence peaks. The peaks also shifted towards lower temperatures with an intensity increase in the lower of the two peaks. The peaks shifted towards the blue spectral region. When the Mn doped $\text{Li}_2\text{B}_4\text{O}_7$ was repeatedly annealed in atmospheric conditions the peaks were partially reduced, whereas in cyclic annealing in the reducing environment followed by annealing in the oxidizing environment, irreversible deformations occurred in the crystal. The deformations prevented reverse diffusion of the oxygen atoms and could cause the displacement of the Mn ion positions and change the charge of the Mn ions. This caused a decrease in the concentration of trap levels. It was determined that during the reduced oxygen annealing environment, oxygen vacancies are produced at the “bridge” O₄ atoms which binds the two tetrahedric boron-oxygen blocks in the anon sublattice. This oxygen vacancy charge compensation takes place due to the reduction of the lithium and manganese ions producing a change in the color spectrum. [8]

The effects of irradiation on photoluminescence and the optical absorption of Mn doped $\text{Li}_2\text{B}_4\text{O}_7$ proved it as a dosimetric material for radiation monitoring. After irradiation with a 1.0

$\times 10^3$ and 1.20×10^4 Gy from a high-energy, short time electron pulse of a linear electron accelerator, the valence states of the Mn changed. The most likely ionization is Mn^{2+} becoming $Mn^{3+} + e^-$ with the electron being captured in a trap. The absorption peak occurred at 3700 Å for the non-irradiated sample. Absorption peaks of 2310 and 2300 Å occurred for the 1.0×10^3 and 1.20×10^4 Gy dose samples respectively.[21]

Recently cathodoluminescence studies of $Li_2B_4O_7$ isovalently doped with K, Ag, and Cu were conducted to evaluate the influence of doping on $Li_2B_4O_7$'s luminescence properties. The cathodoluminescence was conducted both at room temperature and at liquid nitrogen temperatures; the electron beam was pulsed for 3 μ s with a repetition rate of 20 Hz. Using a 9.5 keV electron gun and beam current of 200 μ A, an asymmetric room temperature peak was observed at 3400 Å. At 80 K two emission peaks at 3620 and 5640 Å were observed. The main cathodoluminescence peak of undoped $Li_2B_4O_7$ is the annihilation of a self trapped exciton near self trapped defects. The electron hole pair formations occur at the same time of impurity luminescence emission. F type centers are formed from oxygen vacancies, but F centers are not formed in $Li_2B_4O_7$ since B-O is a strong covalent bond and a strong framework in the crystal lattice. The electron gun's kinetic energy was not high enough to displace oxygen atoms from the molecule. If it was not a tetraborate complex that formed during crystal growth, then F centers are possible where an anion pseudo vacancy occurs. An "anion pseudo vacancy" with a captured electron forms "pseudo F center". In the "pseudo F center", the location of the captured electron is unknown. These "pseudo F centers" only appear at low temperatures at 5640 Å.[22]

Photoemission, inverse photoemission, and angle resolved photoemission of (110) and (100) $\text{Li}_2\text{B}_4\text{O}_7$ was researched to enhance neutron detection capability. The $\text{Li}_2\text{B}_4\text{O}_7(110)$ and $\text{Li}_2\text{B}_4\text{O}_7(100)$ crystal surfaces were band mapped and the binding energies of the Li 1s and O 2s core levels were confirmed. The band gap was determined to be between 9 to 10 eV. The occupied states were extremely flat and the dispersion of occupied states was in determinant. There is a lighter charge carrier effective mass in unoccupied states. A bulk band gap surface state and image potential state in $\text{Li}_2\text{B}_4\text{O}_7(110)$ is present indicating a defect-free surface. Defects due to the O vacancies were found in the $\text{Li}_2\text{B}_4\text{O}_7(110)$ crystal. [4]

Present cathodoluminescence and photoemission research will provide a more in-depth understanding of Mn doped $\text{Li}_2\text{B}_4\text{O}_7$. Current band gap knowledge in undoped and doped $\text{Li}_2\text{B}_4\text{O}_7$ gathers information from having excited electrons above the band gap and observing their relaxation transitions measuring less than 6 eV. A spectrometer and sample chamber completely under vacuum will allow for observed transitions below 2000 Å (above 6 eV). This will allow for observation of all the transitions in the band gap of 9-10 eV. The NIM photoemission will confirm or deny the presence of impurities from the valence band edge to E_{fermi} . Finally, the TGM photoemission will probe into the core states and valence band of Mn doped $\text{Li}_2\text{B}_4\text{O}_7$ confirming the presence of Mn and its energy level in the crystal.

Methodology

A cathodoluminescence system and two separate photoemission systems were used to study undoped and Mn doped $\text{Li}_2\text{B}_4\text{O}_7$. In the cathodoluminescence experiment, although the sample was in vacuum, the optical system and spectrograph were in air, thus limiting spectral data to a minimum wavelength of 1800 Å or a maximum energy of 6 eV, i.e., 4 eV below bandgap. Also, the monochromator's grating was only rated for 2200 to 6000. The photoemission data was collected on two different photoemission systems at CAMD. The first set of data was collected on the TGM photoemission system with higher photon energies and a focus on the location of the Mn and the deeper states of Mn doped $\text{Li}_2\text{B}_4\text{O}_7$. Secondly, the NIM photoemission system was utilized at lower photon energies and focused primarily on the valence band edge of Mn doped $\text{Li}_2\text{B}_4\text{O}_7$.

Cathodoluminescence

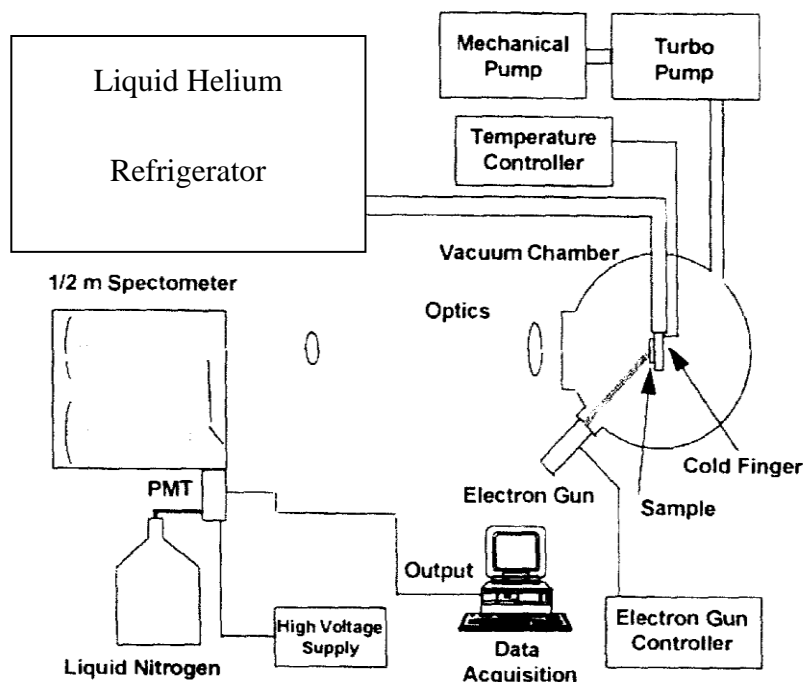


Figure 8. Cathodoluminescence System [23]

The cathodoluminescence system consists of a Kimball Physics EMG-12 electron gun powered by an EGPS-12 power supply, a vacuum system, a liquid helium refrigerator cooled sample holder, a sample chamber with suitable optical ports, an optical system, a spectrometer, and a detector. A sample is placed at the focal point of the electron gun and the resulting cathodoluminescence signal from the sample is transmitted through the quartz window of the vacuum chamber and focused by an optical system onto the entrance slit of the monochromator and then to the photomultiplier or a solid state detector, amplified, and recorded.

The electron beam is incident at an angle of approximately 45^0 with energies between a few hundred eV and several KeV. The incoming electrons act to stimulate photon emission from the $\text{Li}_2\text{B}_4\text{O}_7$. Once the electrons enter the $\text{Li}_2\text{B}_4\text{O}_7$, the $\text{Li}_2\text{B}_4\text{O}_7$ charge redistributes and this interaction with the electrons in the crystal lattice can cause scattering, both elastic and inelastic. Inelastic scattering can cause a well-defined energy loss of the incident electron, and such energy losses can result in single-particle and collective excitations of host electrons. These excitation processes thus excite the electrons in the sample and when these electrons return to their ground state result in photon emission. These photons are produced from the relaxation of the excited electrons back to the ground state between the energy levels of the $\text{Li}_2\text{B}_4\text{O}_7$.

The CL excitation source is a Kimball Physics EMG-12 Electron Gun and an EPGS-12 power supply. This gun can be adjusted from 0 eV to 20 KeV with currents ranging from 10 nA to 100 μA . The electron beam causes the excitation of the sample. As seen in Figure 13, a direct current electron gun consists of a cathode, a control grid, focusing anodes, accelerating anodes, and deflection plates. Electrons are emitted from the heated cathode and are accelerated to the relatively higher positive potential anode. The control grid controls the brightness of the spot on the screen hence controlling the number of electrons that arrive at the anode. A focusing anode controls the size of the irradiated spot on the sample. The vertical and horizontal deflection plates use an electric field to deflect electrons in the vertical and horizontal direction.[\[12\]](#)

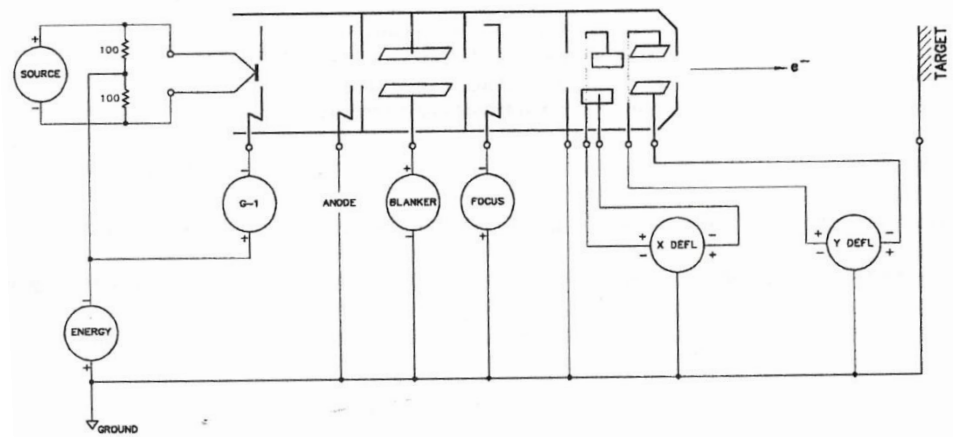


Figure 9. EMG-12 Electron Gun Block Diagram

There are several reasons why an ultra high vacuum system is required for cathodoluminescence. As the level of vacuum is increased the number of gas molecules on the surface decreases, therefore providing a clean surface. The most common and reliable systems utilize two pumping devices. This system utilizes a turbomolecular pump, an ionization gauge, a thermocouple gauge, and a mechanical forepump providing a vacuum in the low 10^{-7} Torr range. The system was usually pumped overnight before measurements were made.

The purpose of the cryogenics is to remove lattice and acoustical phonon vibrations. Liquid nitrogen can cool the sample to 77 K while liquid helium cools the system from room temperature to approximately 4.2 K.

The sample was placed on a brass sample holder mounted in contact with the cryogenic cold finger of the liquid helium refrigerator. Several samples of approximately 0.5 cm x 0.5 cm can be mounted on the sample holder. Two brass strips were mounted at the top or bottom edges of the samples to dissipate charge and conduct heat away. Charge buildup was particularly

acute for the $\text{Li}_2\text{B}_4\text{O}_7$ due to its strong insulator properties. As the light signal passes through the chamber's quartz window, the luminescence is focused using two convex lenses, one placed one focal length from the sample and a second placed one focal length from the spectrometer slit.

The spectrometer provides a measure of the wavelengths and energies of the photons in the emission spectrum from the sample. The Czerny-Turner monochromator consists of a plane grating illuminated by collimated light. The incident light diverges from the slit, is collimated by a concave mirror, incident on the plane grating where the light is diffracted and focused by a second concave mirror onto an exit slit. Each wavelength of light is focused to a different position at the slit, and the wavelength which is transmitted through the slit depends on the rotation angle of the grating. Rotating the grating creates a band of colors leaving the exit slit at different wavelengths. The spectrometer used had a grating with 1200 lines per mm and was blazed at 3000 Å. A schematic of the spectrometer used in this study is shown in Figure 10.

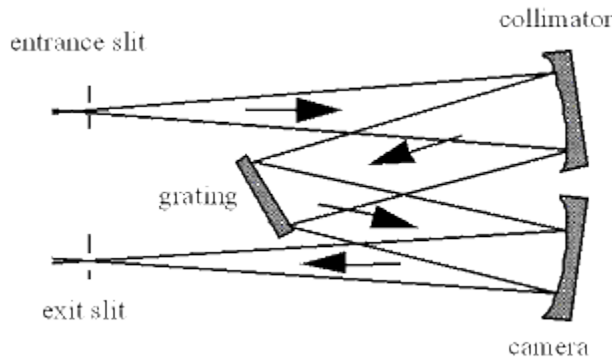


Figure 10. Czerny-Turner spectrometer [24]

Grating performance is also dependent on angular dispersion. Dispersion is the measurement of the angular or spatial separation between the diffracted light of different

wavelengths.[24] To increase angular dispersion, D , one must utilize a grating with a small d or work in higher diffraction orders, m , since

$$D = \frac{d\beta}{d\lambda} = \frac{m}{d \cos \beta} = \frac{\sin \alpha + \sin \beta}{\lambda \cos \beta}. \quad (25)$$

Therefore angular dispersion is dependent on the angles of incidence and diffraction. Linear dispersion is the product of angular dispersion, D , and the effective focal length, f , of the system.[24] As the focal length increases, the linear dispersion improves since

$$f * D = \frac{mf}{d \cos \beta} \quad (26)$$

The maximum resolution or resolving power of the grating is a measurement of the grating's ability to separate adjacent spectral lines of a specific wavelength. The resolving power, R , is

$$R = \frac{\lambda}{d\lambda} = mN \quad (27)$$

where $d\lambda$ is the limit of distinguishable resolution between two equal intensity wavelengths and N is the total number of grooves illuminated on the surface of the grating. [13] For cathodoluminescence spectra with wavelengths from 2200 to 6000 Å, the diffraction grating was an aluminum coated, parallel groove, constant pitch Horiba Scientific grating with 1200 grooved lines per millimeter.[25]

Light input into the spectrometer is especially important with a weak signal. To increase grating efficiency at a specific wavelength, gratings are blazed at a certain angle, θ_b . The

maximum intensity of diffracted light maximum intensity is determined for the direction in which the grooves act as a mirror. The blaze angle relates to the blaze wavelength by

$$m\lambda = 2d \sin \theta_b . \quad (28)$$

Grating efficiency is determined by the blaze condition or the blaze angle.[13] The Horiba Scientific grating was blazed at $11^\circ 25'$ for a maximum efficiency at a wavelength of 3300 Å.[25] Figure 11 provides the relative efficiency of the Horiba Grating for various wavelengths for both a transverse magnetic and transverse electric field polarization.

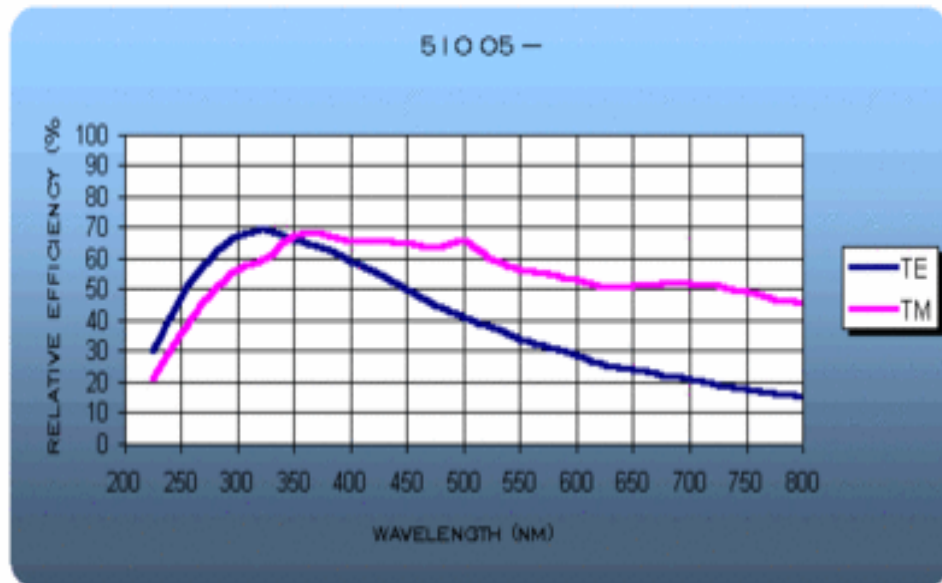


Figure 11. Relative Grating Efficiency for the Horiba Scientific Grating [25]

Calibration of the Czerny-Turner spectrometer was completed with a mercury lamp. The spectrometer slits were set to $10 \mu\text{m}$ and three standard lines for mercury were recorded. Once accurate peaks for the mercury lamp were established, a standard scan covering the three peaks was run and compared to the standard Hg calibration spectra.

The head on photomultiplier tube contains a photocathode followed by focusing electrodes called dynodes and an electron collector or anode all in a vacuum tube as seen in Figure 12.

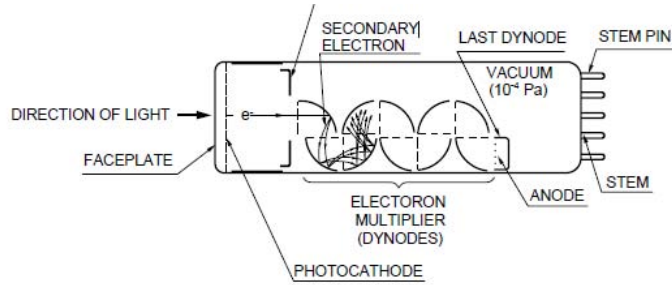


Figure 12. Head-On Type PMT

Photons from the spectrometer are incident on the GaAs photocathode, which ejects electrons with energies greater than the work function of the photoemissive material into the dynode structure.[13] At each dynode typically 3-10 electrons are created by secondary emission. The total amplification or number of electrons at the anode per incident photon, G_e , is dependent on the number of secondary electrons ejected per dynode, δ , and the number of dynodes present.[13]

$$G_e = \delta^d \quad (29)$$

These multiplied electrons are collected by an anode and produce an output signal as a current in the picoampere to microampere range.

The spectral response is dependent on the photoemissive material, in this case, GaAs, which has a nearly flat spectral response between 2000 and 8500 Å. There is a small dark current that flows through the photomultiplier when no photons are present. One source of dark

current is from thermionic emissions of electrons from the photoemissive cathode material. To minimize the dark current, the photomultiplier tube was cooled to -30°C with liquid nitrogen. Other sources of dark current are ionization of residual gases and gas scintillation. The peak quantum efficiency of the GaAs cathode is 25% with a dark current of 10^{-16} Å/cm².[13] The photomultiplier was usually operated at an applied voltage of 1200 volts.

Data was analyzed using the Syner-JY program. In a typical experiment a process called “data preview” was first run to acquire the signal, assist in adjusting the electron beam position on the sample and maximize the signal to noise ratio. The x, y deflection, integration time and slit width were varied in this step to maximize the signal. The smallest slit width that provided an identifiable signal was used to run each experiment. After maximizing the signal using “data preview”, continuous scans were performed at predetermined sample temperatures, beam energies and currents, and spectrometer slit widths using the selected integration times and wavelength intervals in order to obtain the desired cathodoluminescence spectra needed to characterize the Mn doped Li₂B₄O₇.

Photoemission Spectroscopy

Two types of photoemission systems will be discussed; one using a NIM, or normal incident monochromator, and one using a TGM, or toroidal grating monochromator. Both systems provide a tunable photon source for energy dependence and bulk measurements, a plane-polarized light source for characterizing the type of molecular orbitals present, and a very high brightness source. Both of these systems utilize the synchrotron ring at the Center for Advanced Microstructures and Devices (CAMD) of the Louisiana State University in Baton Rouge, LA.

Figure 13 is a schematic of the 3-m toroidal grating monochromator beam line at CAMD. Polarized photons travel through several shutters, and mirrors from the synchrotron ring to the monochromator and then onto the Mn doped $\text{Li}_2\text{B}_4\text{O}_7$ in the vacuum chamber. The photoelectrons are analyzed with a hemispherical energy analyzer, the signal is enhanced and detected by a channel electron multiplier, and the resulting data stored in a computer. [4]

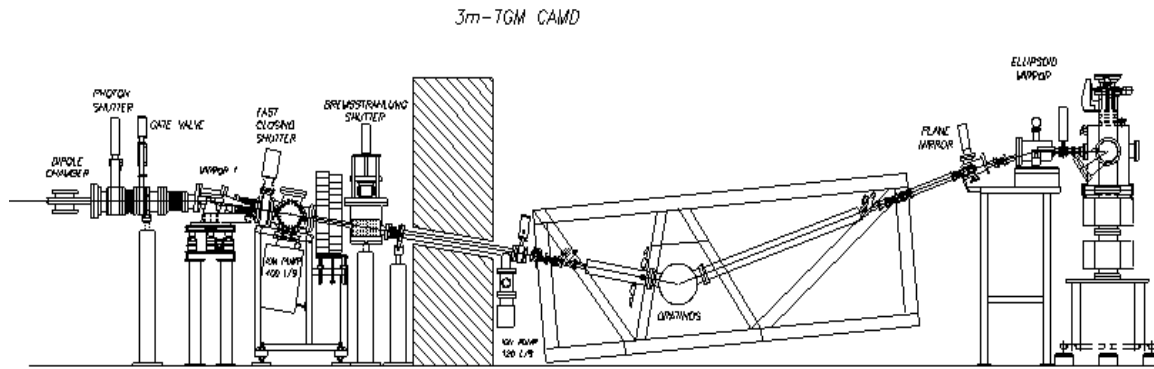


Figure 13. 3m-TGM photoemission line at CAMD.

Figure 14 shows the NIM beamline at CAMD. The electrons exit the ring and supply 70 mrad of radiation to the water cooled ellipsoidal mirror, M_0 . Two cylindrical mirrors, M_1 and M_2 produce an image at the slit. The electrons then strike the surface of the McPherson monochromator grating and are refocused with an ellipsoidal mirror, M_3 , onto the sample in the vacuum chamber. Emitted photoelectrons are then analyzed with a Scienta electron energy analyzer. Finally, a spectra is obtained from the electron current reaching the detector.

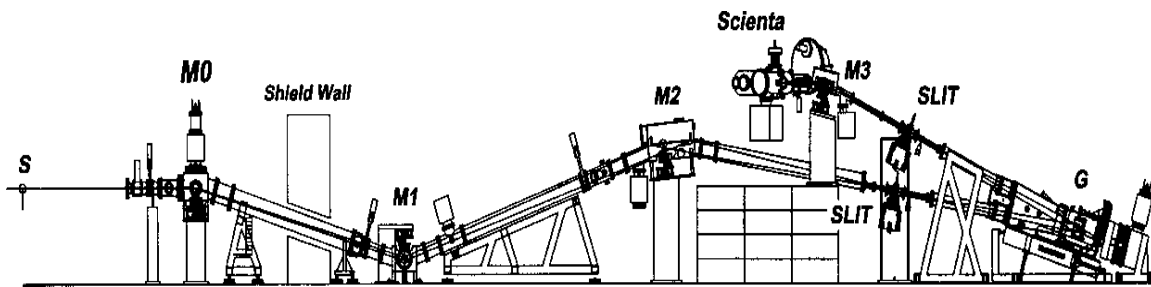


Figure 14. NIM photoemission line at CAMD

The Photoemission Spectroscopy System

There are two photoemission spectroscopy systems utilized at the Center for Advanced Microstructures and Device (CAMD) at Louisiana State University. The TGM beamline has a resolution of 30 to 130 meV and a photon operational range of 15 to 180 eV. The NIM system utilizes photon energies of 2-50 eV with a 10 meV resolution. The NIM system was used to examine Mn doped $\text{Li}_2\text{B}_4\text{O}_7$ from E_{fermi} to the valence band edge with high resolution. The TGM system was used to analyze the Mn doped $\text{Li}_2\text{B}_4\text{O}_7$ from the core electron states to the valence band edge but with a less detailed image.

In both photoemission systems, samples were held in position by welding tantalum wires around the Mn doped $\text{Li}_2\text{B}_4\text{O}_7$ onto a tantalum sample mount. The Mn doped $\text{Li}_2\text{B}_4\text{O}_7$ was cleaned with ethanol and then 75% of the surface was sprayed with Aquadag, a graphite paint, to reduce charging of this wide band gap material. The Mn doped $\text{Li}_2\text{B}_4\text{O}_7$ was then placed in a preparatory chamber sputtered with argon gas for approximately five minutes to clean the surface and then annealed to 450°C to create a smooth surface. Figure 15 represents the preparatory, exchange, and sample chamber on the NIM photoemission line at CAMD.

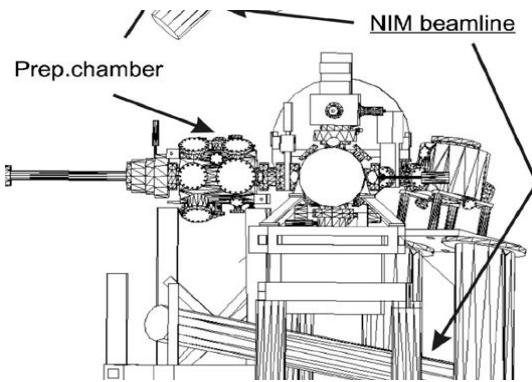


Figure 15. Preparatory, exchange, and sample chamber on the NIM line at CAMD

Source.

Synchrotron radiation, or electromagnetic radiation, is produced from charged particles such as electrons when they travel in curved paths. When the electrons are of high energy and are curving in a magnetic ring, the resulting radiation is intense from the infrared to the x-ray region of the electromagnetic spectrum. A linear particle accelerator is used to provide the beam of particles for the ring. With a linear accelerator particles are accelerated in a straight line by utilizing an array of alternating high energy plates or drift tubes. When particles draw near the plate, they accelerate towards the plate due to the opposite polarity charge applied to the plate. Once the particles pass through a hole in the plate, the polarity is switched. This repels the particles from the initial plate and accelerates it towards the next plate. In this manner the particles eventually reach nearly the speed of light.

The synchrotron ring's beam must be in a vacuum chamber where the pressure is 10^{-9} or 10^{-10} Torr to prevent collisions between residual gas molecules and the circulating electrons. In a storage ring of synchrotron radiation electrons circulate at the speed of light on closed orbitals for several hours emitting radiation from all curved parts of the ring. There are tangential ports

from the ring where small quantities of the radiation leave the ring to experimental stations.

Figure 16 is an overhead representation of the synchrotron ring at CAMD displaying the internal source ring, protective wall, and the tangential lines for experiment stations.[26]

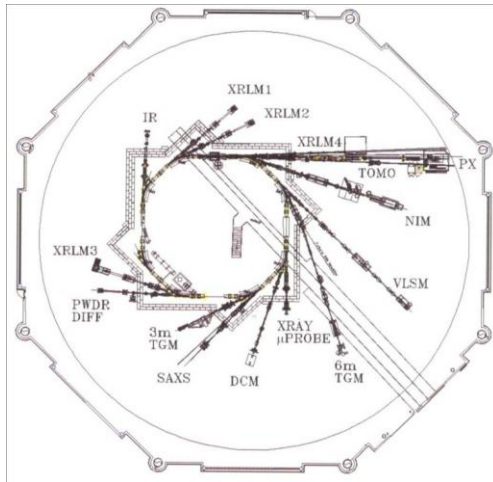


Figure 16. Center of CAMD Synchrotron Ring

3-m NIM Instrumentation.

The 3-m NIM has a 1200 g/mm grating, a dispersion of .28 nm/mm and a resolution of full width half maximum of .005 nm. It utilizes spherical gratings, near normal incident angles, and 3 meter source and objective arms in order to reduce spherical aberrations from the grating source. [26]

When the photons in the synchrotron beam impinge on the $\text{Li}_2\text{B}_4\text{O}_7$ sample mounted in the sample chamber, photoelectrons are released. The Scienta electron energy analyzer receives these photo electrons which pass through a slit from the sample chamber. In the analyzer, the electrons are reflected at a small angle by a retractable cylindrical mirror. This reflection plane

of incidence is small and is orthogonal to the plane of incidence of the incoming electrons. Then a toroidal mirror reflects the electron beam vertically producing a horizontal output beam.

TGM Photoemission System.

The TGM used a 50 mm hemispherical electron analyzer. Electrons enter the analyzer through a small slit and are bent by an electrostatic potential. This electrostatic potential of $1/r$ is applied between the two hemispherical metallic walls. Altering the electric field filters the photoelectrons emitted from the sample. Only electrons of a specific energy and angle are able to enter the analyzer and are focused on the exit slit.[4] The photoelectrons were amplified and counted using a channel electron multiplier.

Analysis and Results

Chapter Overview

In this chapter, analysis of the photoemission and cathodoluminescence spectra of $\text{Li}_2\text{B}_4\text{O}_7$ and Mn doped $\text{Li}_2\text{B}_4\text{O}_7$ will be provided. The cathodoluminescence data was collected on a single experimental system located at AFIT whereas the photoemission (PES) data was collected on two different photoemission systems at CAMD. The first set was collected on the TGM photoemission system which utilized higher incident photon energies and lower energy resolution. These measurements focused primarily on the Li and O s-states as well as the valence band edge of Mn doped $\text{Li}_2\text{B}_4\text{O}_7$. The second set of PES data was collected on the NIM photoemission system which provided for lower incident photon energies and higher energy resolution useful for studying the valence band and the valence band edge states to determine the role that Mn plays.

Origin software was used for fitting the experimental data with a minimum number of Gaussian distributions. In cathodoluminescence, each peak represents a photon emission in the band gap. For photoemission each peak represents a particular molecular orbital or core electron.

Results of Simulation Scenarios

CASINO modeling utilizing Monte Carlo simulations was used to determine electron penetration depth, location, and the energy absorbed in the Mn doped $\text{Li}_2\text{B}_4\text{O}_7$.^[27] Assuming a Gaussian shaped electron beam with a 20 nm electron beam diameter emitting 200,000 electrons

at 10 KeV, Figure 17 represents the penetration depth of the electrons. The red electrons are backscattered towards the surface and only penetrate approximately 400 nm into the surface. The blue electrons are concentrated towards the surface with a maximum penetration depth of approximately 1400 nm. Electrons with energies greater than 50 eV are considered to have escaped the surface. Since the Mn doped $\text{Li}_2\text{B}_4\text{O}_7$ is thicker than 1400 nm, the incident electrons are not transmitted through the depth of the sample.

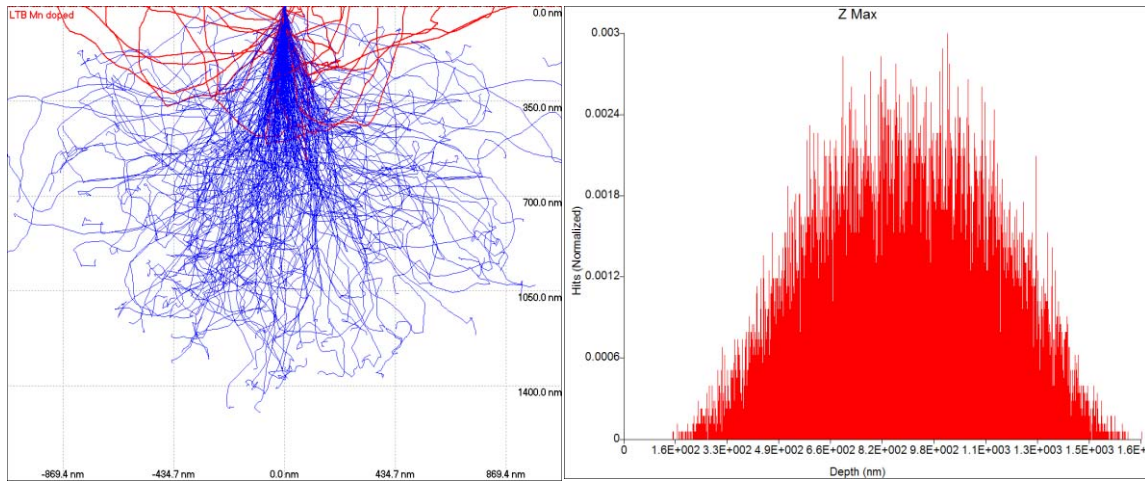


Figure 17 (Left). CASINO model of electron penetration depth in Mn doped $\text{Li}_2\text{B}_4\text{O}_7$ with 10 KeV electron gun, 200,000 electrons, and a 10nm beam radius. **(Right)** Maximum electron penetration depth in Mn doped $\text{Li}_2\text{B}_4\text{O}_7$.

Figure 17 is a CASINO output representing the electron penetration depth and indicating that the electrons penetrate in a Gaussian distribution with maximum penetration between 660 and 1100 nm, hence not transmitting through the crystal. Figure 18 represents the electron energy lost in the sample as a result of characteristic x-ray production. The $\phi(\rho Z)$ curves depict the radial distributions of the x-rays generated for the boron, oxygen, and manganese components of $\text{Li}_2\text{B}_4\text{O}_7$ by the K and L III shell electrons. This flux of x-rays is produced as the

electrons interact with the K and LIII shell electrons in the respective atoms. As a result of this interaction the incident electrons are slowed down. These x-ray distributions demonstrate that most of the x-rays are produced near the surface of the crystal. Boron produces most x-rays from K shell electrons at the surface and quickly decays beyond the surface. Oxygen K shell x-rays gradually increase to a maximum at approximately 300 nm and gradually decrease to zero 1,600 nm into the surface. Likewise, for Mn, the K shell and L shell x-rays both peak at 1700 nm from the surface and gradually decrease as well. From Figure 18, it is clear that Mn doped $\text{Li}_2\text{B}_4\text{O}_7$ has the greatest x-ray intensity near the surface with the greatest intensity resulting from the K shell oxygen electrons.

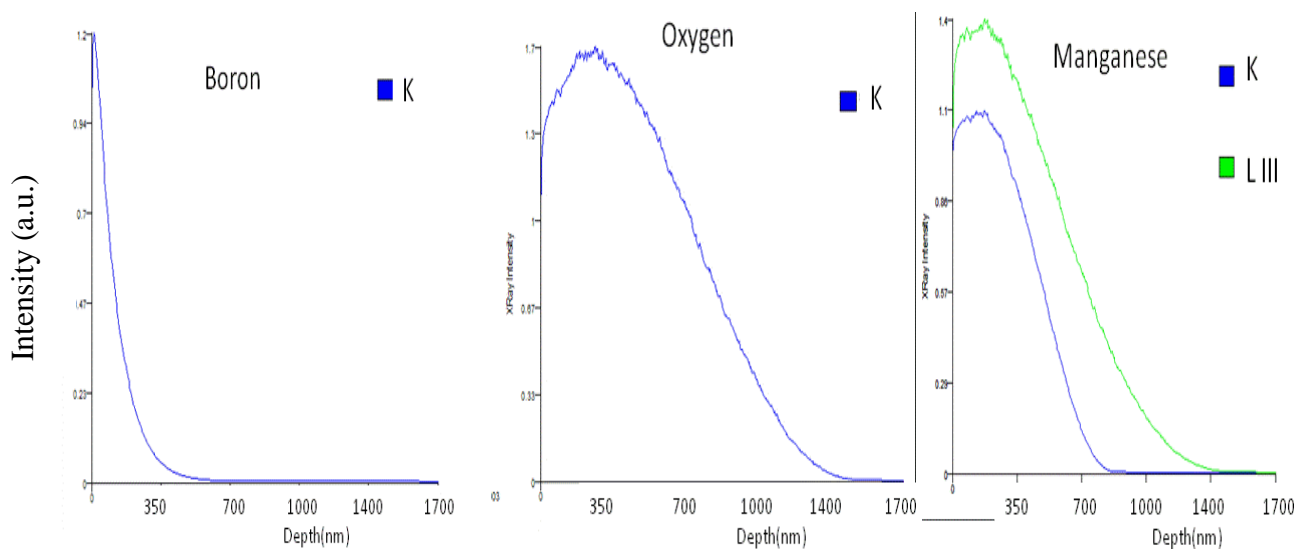


Figure 18. $\phi(\rho Z)$ curve of Mn doped $\text{Li}_2\text{B}_4\text{O}_7$ at 10 KeV with 200,000 projected electrons

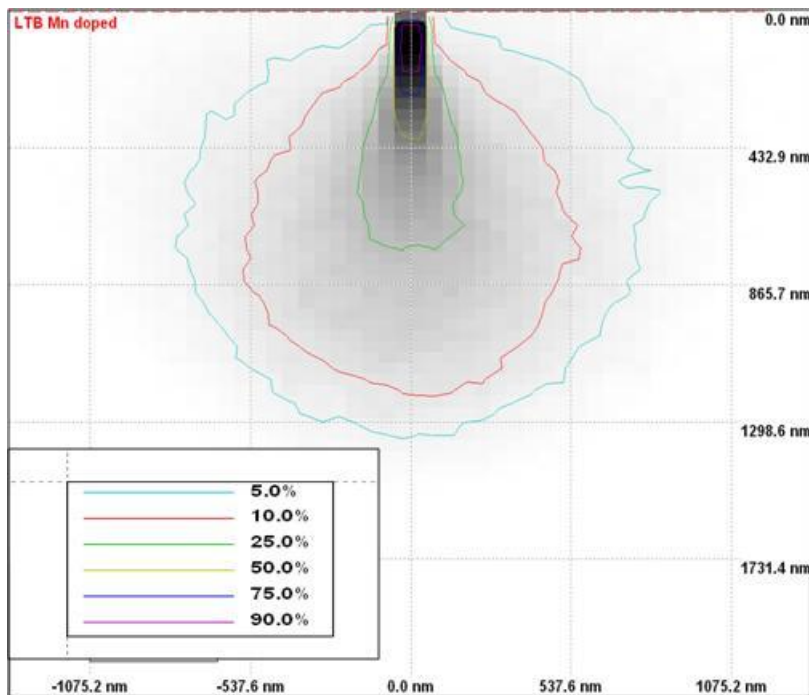


Figure 19. Cross-section view of absorbed energy in Mn doped $\text{Li}_2\text{B}_4\text{O}_7$ sample with 10 KeV accelerating voltage

Figure 19 depicts the energy of the electrons as a function of position in the Mn doped $\text{Li}_2\text{B}_4\text{O}_7$ and thus shows where the energy is absorbed in the sample. Only 5% of the energy reaches a depth of 1300 nm. As predicted by the Kanaya and Okayama model, approximately 90% of the electron energy is deposited near the surface of the sample having penetrated less than 200 nm. This is one of the sources of surface charging.

Crystal Charging

Throughout this research photovoltaic charging has been a significant problem. Charging occurs in the Mn doped $\text{Li}_2\text{B}_4\text{O}_7$ as electrons leave the sample producing an anion. Since Mn doped $\text{Li}_2\text{B}_4\text{O}_7$ has a band gap of approximately 9-10 eV, and is thus an insulator, this positive charge will become fixed forming a positive charged surface layer. This positive surface layer

affects both photoemission by generating a space charge or a columbic potential influencing photoelectrons entering the electron energy analyzer in PES and by attracting the incoming electrons in cathodoluminescence.

After long exposure to the electron beam, the $\text{Li}_2\text{B}_4\text{O}_7$ surface becomes darkened. A surface layer of increasing opacity forms with electron exposure. The aged area most likely contains microcrystalline graphite due to the cracking of the hydrocarbon/CO/CO₂ contaminant layer generally present under vacuum conditions. [10] Accumulation of carbon during electron beam exposure at high current densities may cause a decline in the cathodoluminescence signal at low voltages where the maximum electron range is only hundreds of Angstroms. As the hydrocarbons are continuously refreshed, the spot on the samples grows larger and larger. [10]

Surface charging was minimized by several means. First the $\text{Li}_2\text{B}_4\text{O}_7$ samples were inserted on the sample holder between a brass plate and brass bars to dissipate charging. Then, the $\text{Li}_2\text{B}_4\text{O}_7$ samples were coated with a conducting graphite paint leaving a small opening for the electron gun beam to penetrate the sample surface. Finally, the $\text{Li}_2\text{B}_4\text{O}_7$ samples were usually heated above room temperature to decrease charging.

The left picture of Figure 20 represents the surface of the Mn doped $\text{Li}_2\text{B}_4\text{O}_7$ after a cathodoluminescence run when the sample was removed from the chamber. On the premise that the use of vacuum grease to affix the sample to the brass sample holder was the source of the discoloration, its use was discontinued but the discoloration of the surface still occurred. Aerodag, a graphite aerosol paint was added and removed to selected samples but the discoloration was still present. It was believed that the presence of hydrocarbons was

responsible for the charred, pitted, and cracked surface. However the Mn doped Li₂B₄O₇ was analyzed in a new oil free cathodoluminescence chamber and the scarred surfaces remained. The explanation for this charring is not clear at this point but it does seem that the charring is associated with the incident electron beam causing a reaction on the surface of the Mn doped Li₂B₄O₇. The right hand picture of Figure 20 represents the same sample surface after an hour of polishing with a mechanical polisher, a buffing pad, and an abrasive powder.

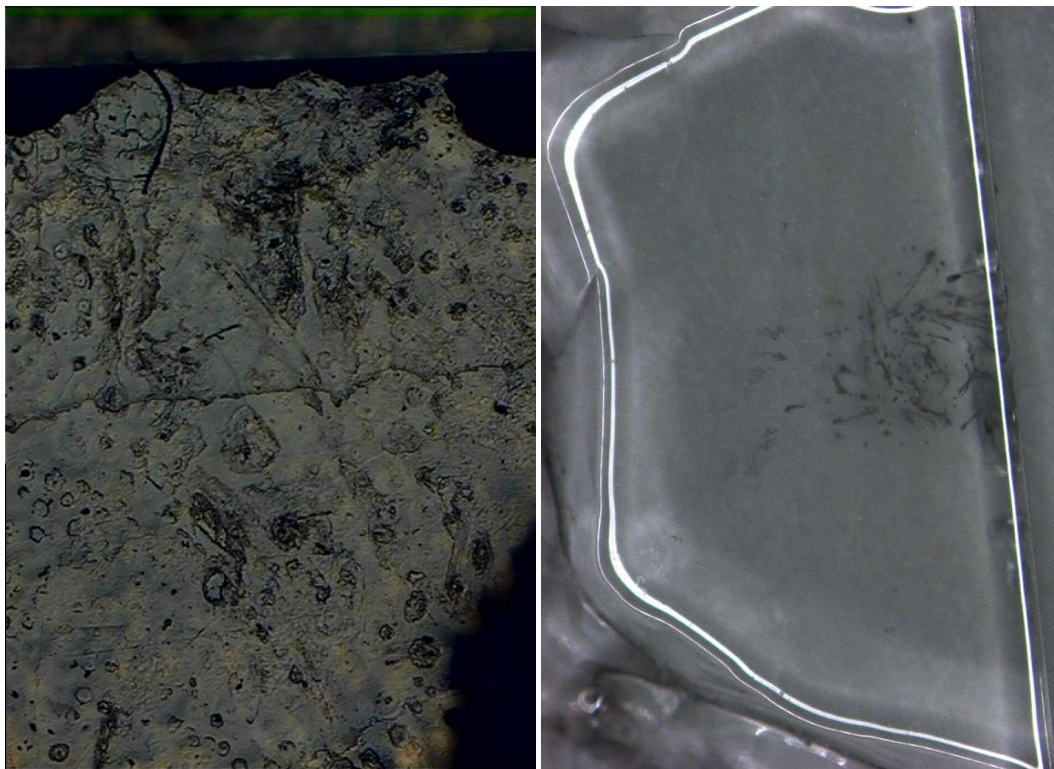


Figure 20. Surface of Mn doped Li₂B₄O₇ after cathodoluminescence. On left surface before polishing and on right the surface after polishing for thirty minutes.

Calibration of the Cathodoluminescence Systems

The cathodoluminescence system's monochromator was calibrated with an Oriel Spectral Hg calibration lamp at various wavelengths. A mercury lamp was placed at the entrance slit of the monochromator, calibration spectra were run, and the grating on the monochromator was shifted in wavelength to adjust to the standard for Hg. The calibration curve spectrum was taken at room temperature with a 15 μm slit width, a 0.1 second integration time, a 0.1 Å step size, and a cooled PMT. The calibrated wavelengths are compared to the NIST Strong Lines of Mercury (Hg) Chart in Table 1. The Δ , or difference in wavelength is due to the fact that the monochromator inlet and exit slits were opened to 15 μm . If the slits would have been narrowed to approximately 5 μm there would be less deviation from the standard Hg lamp values. The highlighted wavelength is the second order wavelength of the measured 2535.83 Å wavelength.

Table 1. Measured and Standard Wavelengths for the non VUV system

Measured λ (Å)	Standard λ (Å)	Δ (Å)
2535.83	2536.52	-0.687
2967.84	2967.2	0.64
3125.867	3125.67	0.199
3131.5478	3131.55	-0.0002
3132.82	3131.84	0.981
3650.1505	3650.15	-0.00255
4359.097	4358.33	0.769
5071.66	5073.03	-1.374
5461.246	5460.74	0.511
5769.03	5769.6	-0.568
5792.49	5790.66	1.827

Cathodoluminescence Spectra of Undoped and Mn doped Li₂B₄O₇

After calibration, undoped along with Mn, Cu, and Ag doped Li₂B₄O₇ were analyzed as a basis for reference to previously published papers with X-ray luminescence, X-ray Fine Absorption Spectroscopy (XFAS), photoluminescence, radioluminescence, and thermoluminescence.

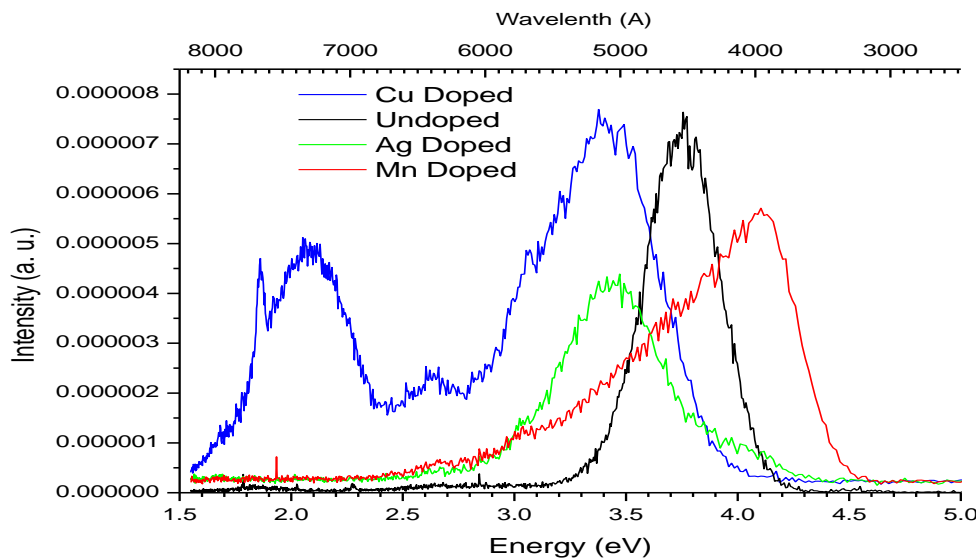


Figure the initial room temperature cathodoluminescence spectra of Cu, Ag, Mn and
undop **Intensity (a.u.)** Li₂B₄O₇. Clearly there is a strong peak ranging from 3.4 to 4.2 eV shifting due to the
dopar Cu spectrum provided additional peaks at 2.1 and 2.3 eV not clearly evident in the
other samples. These peaks may be due to a strong La presence determined by EPR to be in the
Cu doped sample.[28] Due to the presence of other research and publications on Ag and Cu

doped samples, this thesis research focused only on the undoped and Mn doped crystals.

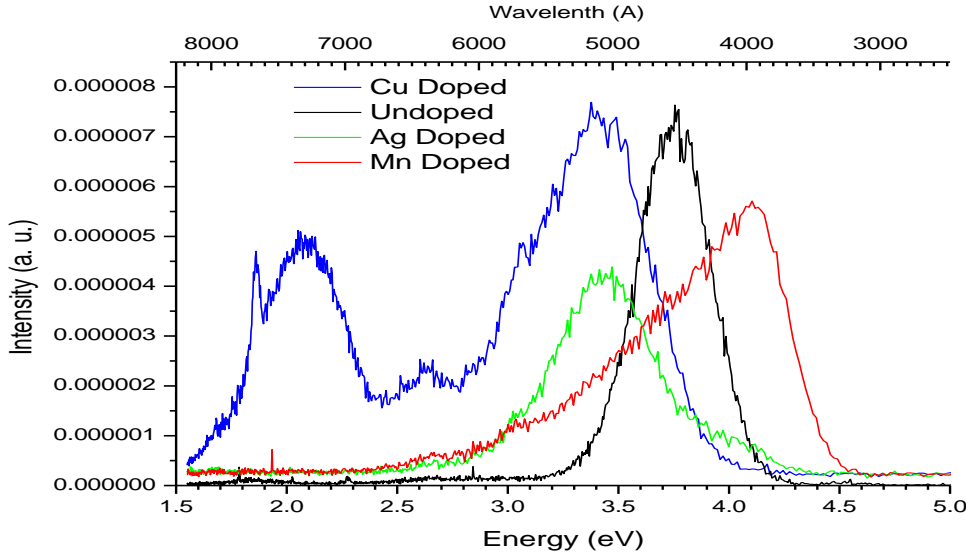


Figure 21. Room Temperature Cathodoluminescence Spectra of Cu, Ag, Mn, and Undoped $\text{Li}_2\text{B}_4\text{O}_7$

All $\text{Li}_2\text{B}_4\text{O}_7$ crystals have relatively strong broad cathodoluminescence peaks ranging from 3.4 to 3.7 eV. Broad intrinsic emission generally results from self-trapped excitons (STE) or highly localized excitons trapped by their own self-induced lattice distortion. STE's are generally produced in crystals with a deformable lattice characterized by strong electron-phonon coupling. The STE's emission energy is usually much lower than the band gap of the $\text{Li}_2\text{B}_4\text{O}_7$ due to phonon energy lost during the electronic transition. [29]

Different types of STEs are a characteristic feature of insulating crystals. STE's decay radiatively from one or more local minima on the adiabatic potential energy surfaces for the

spin-singlet and spin-triplet states of the lowest orbital energy. Fluorescence emission from the singlet state is short lived, but long lifetime luminescence is observed for triplet states. Triplet and singlet STEs can coexist and have overlapping emission bands as can be seen in Figure 22.

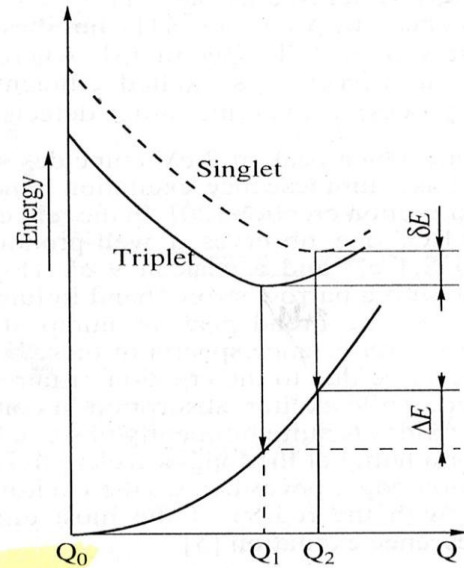


Figure 22. Adiabatic potential curves for STEs in lithium borates.[30]

Excitons rapidly distort the $\text{Li}_2\text{B}_4\text{O}_7$ lattice, altering bond-lengths and localizing in a fixed region. During this exciton self trapping process the exciton distorts the lattice creating dynamical vibration excitations, or phonons. These phonon waves propagate in opposite directions, reflect from the chain ends, and again meet at the site of the exciton, where they delocalize the exciton by pulling it out of its well. The exciton attempts to localize again creating more phonons; energy is exchanged between the electronic and vibrational degrees of freedom. [29]

STE's affect the intrinsic luminescence, energy transport properties, and radiation damage processes of the crystal. In other compounds such as alkali halides, STE's are the

precursors of lattice defects formed by ionizing radiation and laser-induced breakdown damage. STE's involve strong electron lattice coupling associated with covalent bond formation between the lattice constituents that are only reactive in an excited state.[31] The electron beam excitation in cathodoluminescence creates a valence hole and the hole is localized on a new chemical bond occupying the highest antibonding orbital of the bonded pair. The formation of this self trapped hole is necessary for the existence of a self trapped exciton. The STE forms when the conduction electron is bound to the self trapping site.[31]

Recombination of electrons with self trapped holes yields broad band luminescence which is Stokes-shifted by several electron volts from the band edge.[32] These self trapped holes or V_k centers are nonmobile and stable as long as the electrons are trapped at another location in the $Li_2B_4O_7$.

Undoped Single Crystal $Li_2B_4O_7$

The cathodoluminescence spectra of the (100) surface of the undoped sample of $Li_2B_4O_7$ was obtained at room temperature with 50 uA of current and a 5 KeV electron beam. This spectrum, shown in Figure 23 has peaks at approximately 3.1, 3.6, 4.1, and 6.0 eV, peaks believed to be due to self trapped excitons located at O vacancies or interstitial sites. As the incident beam energy increases, the electrons penetrate further into the sample's surface. The first four peaks change in relative peak heights causing a shift in peak strengths. This is caused by a different distribution of STEs; as the energy increased so did the energy of the thermally released STEs.

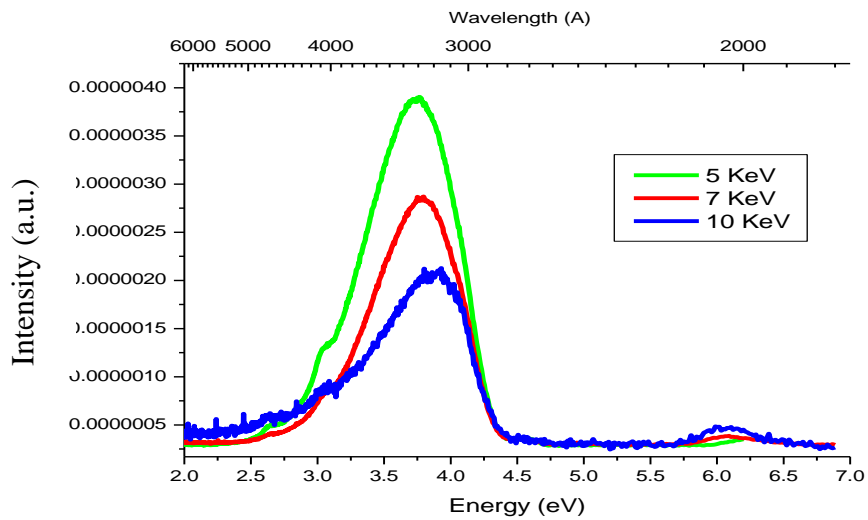


Figure 23. Cathodoluminescence spectrum of (100) $\text{Li}_2\text{B}_4\text{O}_7$ at 5, 7, and 10 KeV, 50 uA of current with 400 um slit width, 1 second integration time and a -31°C PMT

Figure 24 represents the Gaussian fits to the cathodoluminescence spectra of (100) $\text{Li}_2\text{B}_4\text{O}_7$ at 5, 7, and 10 KeV, 50 uA of current, with a 400 um slit width, 1 second integration time and a cooled PMT. It is clear that in the single energy spectra there are four energy peaks. As seen in Figure 23, a weaker intensity peak exists at 6.2 eV probably due to a transition towards the middle of the band gap. This peak is not documented in previous publications. This transition may be between a donor and acceptor pair. Also transitions between deep donors and the valence band, or between the conduction band and deep acceptors would be feasible.

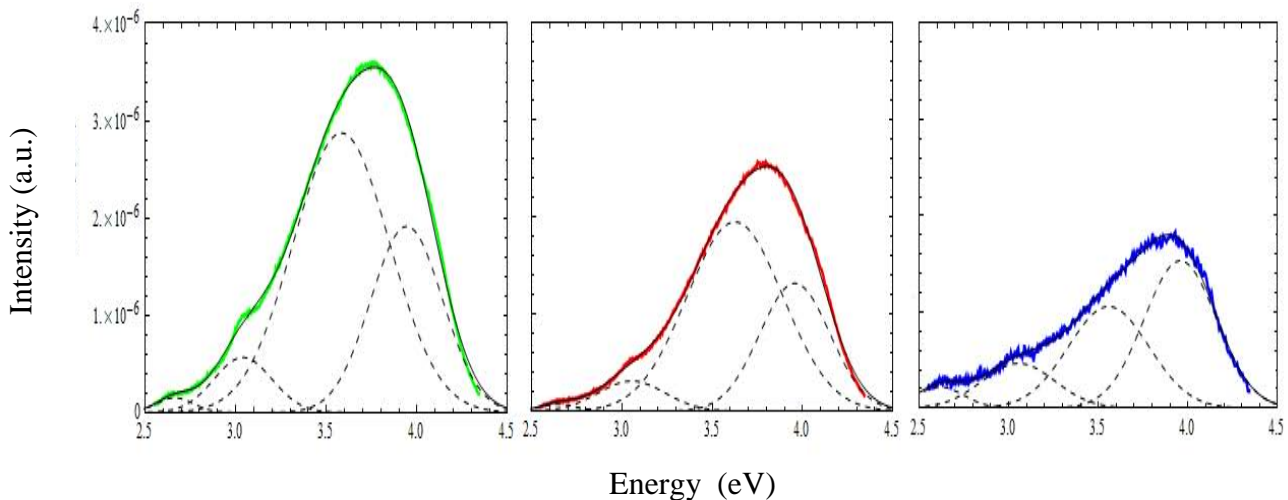


Figure 24. Gaussian distribution of cathodoluminescence spectrum of (100) $\text{Li}_2\text{B}_4\text{O}_7$ at 5, 7 and 10 KeV, 50 uA of current with 1 second integration time, and a -31°C PMT.

Table 2. Mean Gaussian energies for luminescence spectra in Figure 24.

	Gaussian 1	Gaussian 2	Gaussian 3	Gaussian 4
5 KeV	2.617 eV	3.054 eV	3.557 eV	3.957 eV
7 KeV	2.649 eV	3.054 eV	3.626 eV	3.957 eV
10 KeV	2.664 eV	3.040 eV	3.583 eV	3.943 eV

Undoped Amorphous $\text{Li}_2\text{B}_4\text{O}_7$

The CL spectra of amorphous $\text{Li}_2\text{B}_4\text{O}_7$ is in agreement with previous post x-ray irradiation thermoluminescence spectra of undoped $\text{Li}_2\text{B}_4\text{O}_7$ taken at 77-293 K in the AFIT laboratories. This spectrum is shown in Figure 25. The thermoluminescence spectra's energy peaks are in agreement with those in the CL spectra at 2.58, 3.03, and 3.58 eV. At 77K the electrons are trapped at O vacancies and holes are trapped at Li vacancies, both recombining after room temperature annealing. In addition, EPR pre and post annealing studies provided

additional spectra to the thermoluminescence spectra, confirming that the peaks are attributable to oxygen and lithium vacancies.[33]

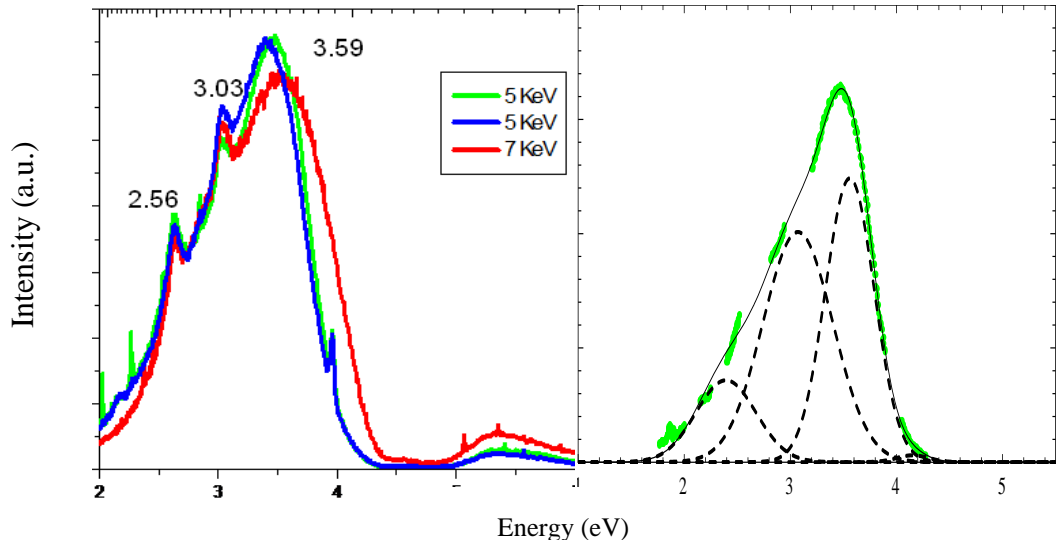


Figure 25. (Left) Cathodoluminescence spectrum of amorphous $\text{Li}_2\text{B}_4\text{O}_7$ at 5 and 7 KeV, 50 uA of current with 1 second integration time, and a -31°C PMT. (Right) Four peak Gaussian fit for the 5 KeV spectra at 2.2438, 2.670, 3.534, and 4.170 eV.

The cathodoluminescence spectra energy peaks of amorphous $\text{Li}_2\text{B}_4\text{O}_7$ at 2.2438, 2.670, 3.534, and 4.170 eV are in agreement with previous post x-ray irradiation thermoluminescence spectra of undoped $\text{Li}_2\text{B}_4\text{O}_7$ taken at 77-293 K in the AFIT laboratories. The sharp peaks at 2.56, 3.03, and 4.0 eV (for 7 KeV only) of the cathodoluminescence spectra in Figure 25 are thought to be contamination in the vacuum chamber. The thermoluminescence spectra's energy peaks at 2.573, 3.102, 3.579, and 3.993 eV are shown in Figure 26. At 77K the electrons are trapped at O vacancies and holes are trapped at Li vacancies, both recombining after room temperature annealing. In addition, EPR pre and post annealing studies provided additional spectra to the

thermoluminescence spectra, confirming that the peaks are attributable to oxygen and lithium vacancies.[33]

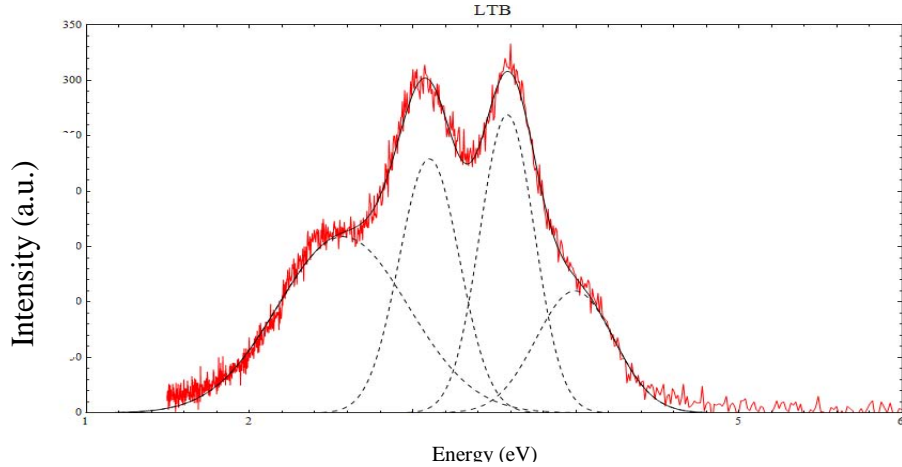


Figure 26. X-ray irradiation thermoluminescence spectra of undoped $\text{Li}_2\text{B}_4\text{O}_7$. Four peak Gaussian fit for the 5 KeV spectra at 2.573, 3.102, 3.579, and 3.993 eV.[33]

Mn Doped Single Crystal $\text{Li}_2\text{B}_4\text{O}_7$

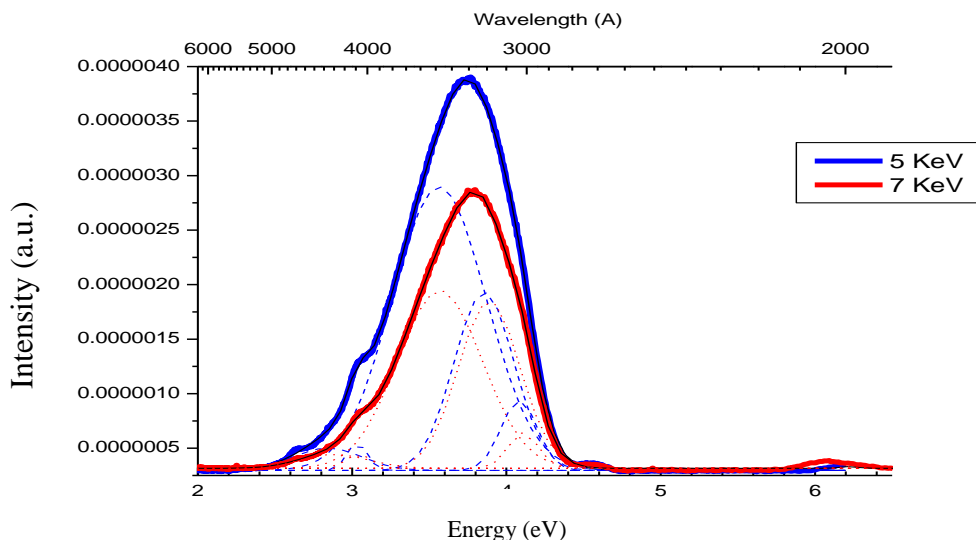


Figure 27. Cathodoluminescence spectrum of single crystal Mn doped $\text{Li}_2\text{B}_4\text{O}_7$ at 5 and 7 KeV, 50 uA of current with a - ^{31}C PMT.

Doped impurity centers such as Mn provide extrinsic trapping sites as alternatives to self trapping. Mn impurity ions may substitute for lithium ions in the $\text{Li}_2\text{B}_4\text{O}_7$ lattice. The Mn ion impurity likely fills a Li vacancy in the $\text{Li}_2\text{B}_4\text{O}_7$ crystal. The atomic radius of Mn is 1.79 Å and atomic radius of Li is 2.05 Å. The ground state Mn^{2+} ($3d^5$) impurity ions can trap free electrons.

It is possible for the Mn atoms occupying the Li sites to act as donors. Primary collision mechanisms in the lattice are impurity scattering and phonon scattering. Since the spectra are collected at room temperature, both phonon and impurity scattering due to defects will be operative. Collisions resulting from such scattering cause an abrupt change in the carrier velocity and the collision time resulting in carrier motion which is semi-random due to frequent changes in direction and velocity. Conductivity, σ , is computed from $\sigma = n e \mu$, where n is the number of electrons, e, is the charge of an electron, and μ is mobility. If the number of Mn impurities increases, the electron carrier mobility will decrease. The increase in n can overcome the impurities resulting in a conductivity increase.

Note that the Mn doped $\text{Li}_2\text{B}_4\text{O}_7$ CL curve presents a slightly narrower peak at approximately 3.7 eV than the undoped $\text{Li}_2\text{B}_4\text{O}_7$. A narrow peak indicates the exciton carrier lifetime, τ , is much longer for the Mn doped $\text{Li}_2\text{B}_4\text{O}_7$. Narrower cathodoluminescence spectra indicate a strong surface component.[34] Since carrier lifetimes or decay times, τ , increase, the Mn is in effect suppressing the surface voltaic charging of the undoped $\text{Li}_2\text{B}_4\text{O}_7$ crystal. This narrowing is a strong indication of increased surface and bulk conductivity with Mn doping. The secondary charge carriers, electrons and holes are free to move for some time at the surface of

the Mn doped $\text{Li}_2\text{B}_4\text{O}_7$. Since mobility, μ , is calculated as $\mu = e \tau / m^*$, where m^* is the effective mass of the electron or hole, an increase in τ will increase mobility.[34]

The enhanced carrier mobility at the surface is in agreement with greater surface conductivity evident in the reduced surface charging. [31] Hence the increased surface mobilities and carrier lifetimes in the Mn doped $\text{Li}_2\text{B}_4\text{O}_7$ are in agreement with the reduction in hysteresis in the surface voltages which will be observed in the photoemission spectra.

Amorphous Mn Doped $\text{Li}_2\text{B}_4\text{O}_7$

Figure 28 shows the cathodoluminescence spectrum of amorphous Mn doped $\text{Li}_2\text{B}_4\text{O}_7$ at 10 KeV, 50 uA of current, 400 um slit width, 1 Å step size and a cooled PMT. As the amount of time that the crystal's surface was impacted with electrons increased, surface charging reduced the signal to noise ratio. In addition, the signal to noise ratio also decreased due to the increasing presence of hydrocarbons on the crystal's surface as time elapsed.

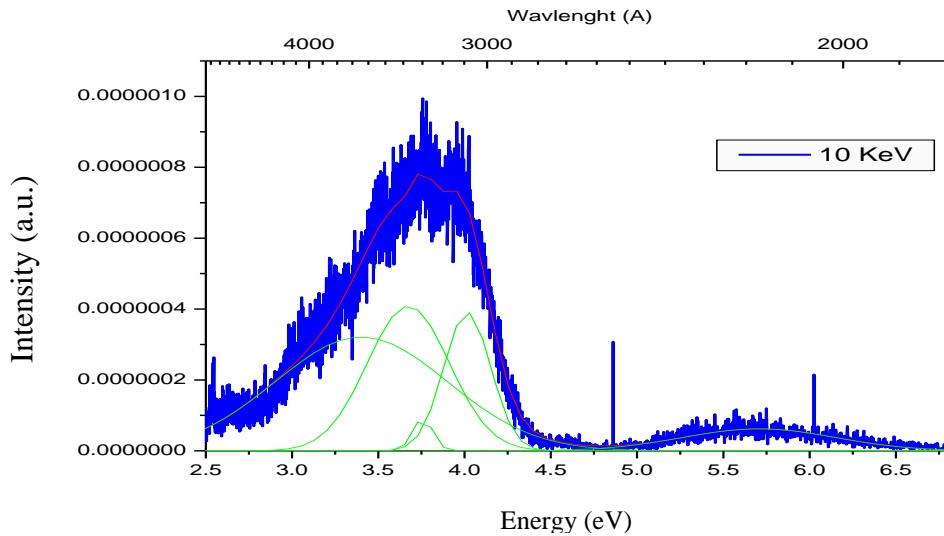


Figure 28. Cathodoluminescence spectrum of amorphous Mn doped $\text{Li}_2\text{B}_4\text{O}_7$ at 10 KeV, 50 uA of current, 400 um slit width, 1 Å step size and a -31°C PMT

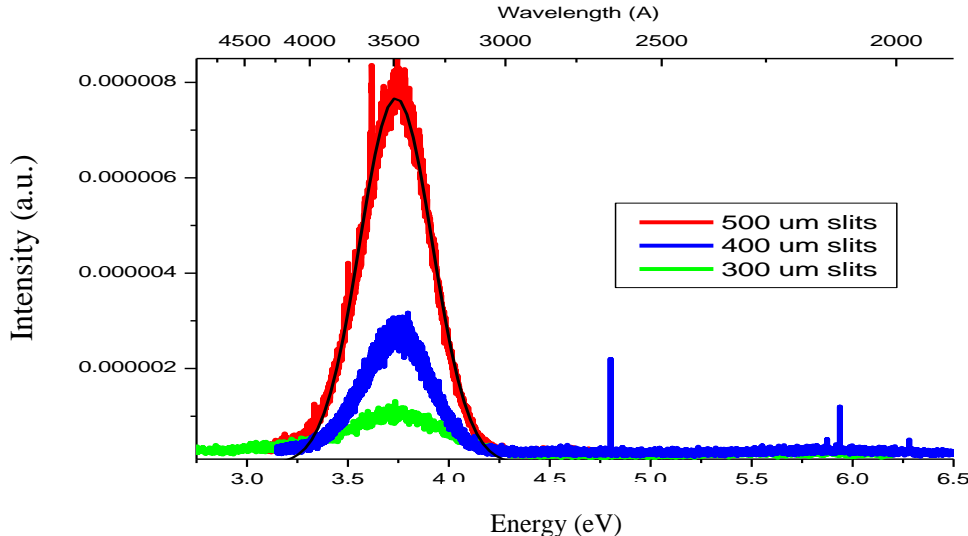


Figure 29. Cathodoluminescence spectrum of amorphous Mn doped $\text{Li}_2\text{B}_4\text{O}_7$ at 10 KeV, 50 uA of current, 300/ 400/500 um slit width, 1 Å step size and a -31°C PMT

Figure 29 is the cathodoluminescence spectrum of amorphous Mn doped $\text{Li}_2\text{B}_4\text{O}_7$ at 10 KeV, 50 uA of current, 300/ 400/500 um slit width, 1 Å step size and a cooled PMT. By increasing the slit width of the monochromator, the signal increased but the primary peak at 3.73 eV remained constant. Not obvious in Figure 29 is another peak at 5.6 eV which is overshadowed by the intensity of the 3.73 eV spectra.

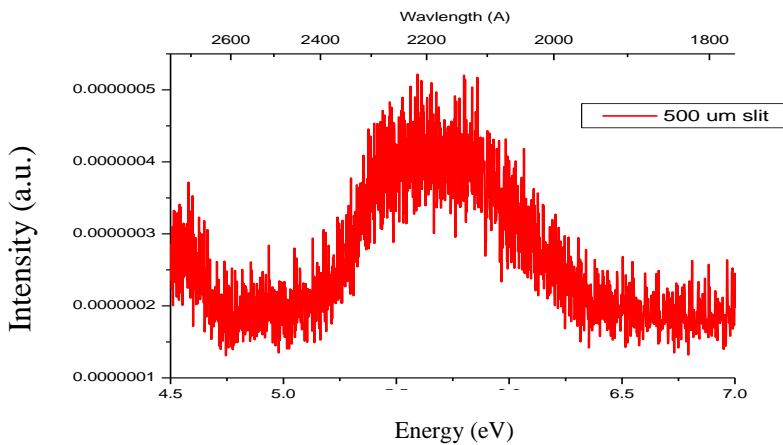


Figure 30. Cathodoluminescence spectrum of amorphous Mn doped $\text{Li}_2\text{B}_4\text{O}_7$ at 5 KeV, 50 uA of current, 500 um slit width, 1 Å step size and a -31°C PMT

Figure 30 is an enlargement of the region between 4.5 and 7.0 eV of the spectrum shown in Figure 29. The weaker intensity peak at 5.73 eV is due to a transition towards the middle of the band gap. This peak is not documented in previous studies but may be a donor-acceptor pair transition. Also transitions between a deep donor and the valence band, or between the conduction band and a deep acceptor might be feasible. Since the band gap is approximately 9.5-10 eV, there should be another transition between 3.77 and 4.24 eV.

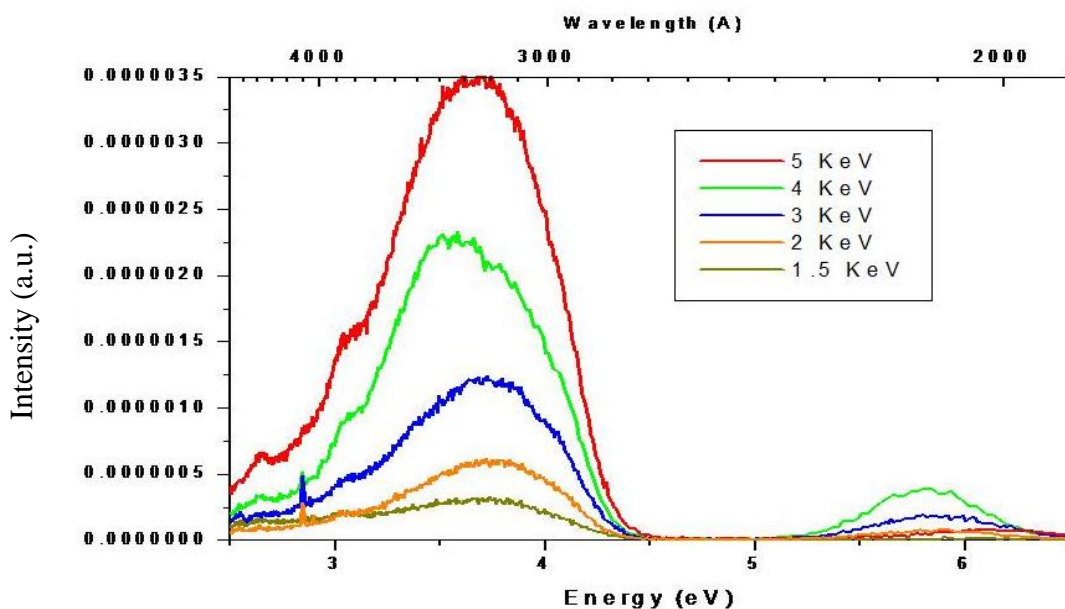


Figure 31. Cathodoluminescence spectrum of amorphous Mn doped $\text{Li}_2\text{B}_4\text{O}_7$ at 5,4,3,2, and 1.5 KeV, 50 uA of current, 1mm slit width, .1 integration time, and a- 31°C PMT

Figure 31 is an energy dependence spectrum of amorphous Mn doped $\text{Li}_2\text{B}_4\text{O}_7$ from 5 to 1.5 KeV. As the energy of the electrons penetrating the crystal's surface is increased, they travel further into the body of the crystal. Since the penetrating electrons remained at the same current, the number of electrons striking the sample remains constant. The primary peak at approximately 3.6 eV shifted slightly to higher energies with increased electron penetration.

Figure 32 is the Gaussian distribution of the 4peaks cathodoluminescence spectrum of amorphous Mn doped $\text{Li}_2\text{B}_4\text{O}_7$ at 5 KeV. All peaks are relatively consistent with previous spectrum of undoped $\text{Li}_2\text{B}_4\text{O}_7$. It can be inferred the Mn in the Mn doped $\text{Li}_2\text{B}_4\text{O}_7$ provided little to no input to the cathodoluminescence spectra.

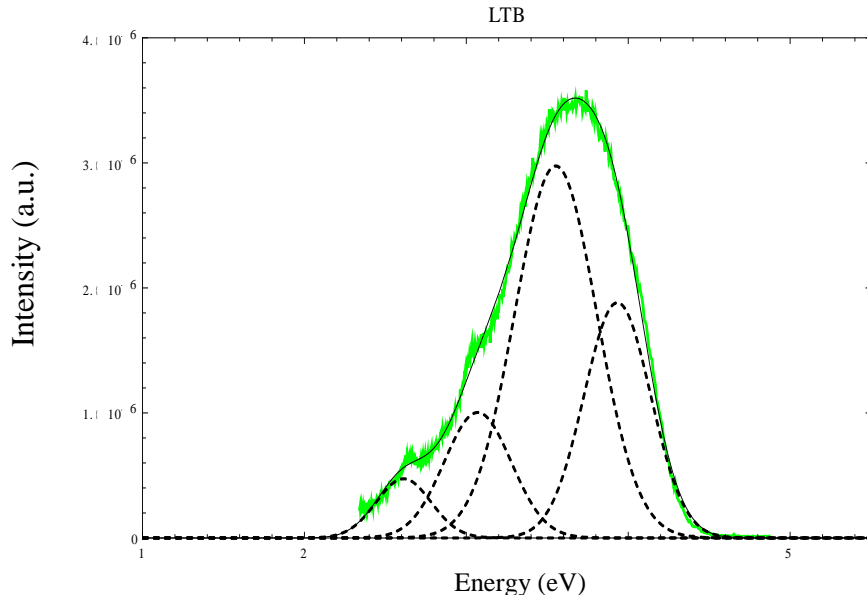


Figure 32. Four peak Gaussian fit for the 5 KeV spectra at 2.710, 3.035, 3.513, and 3.932 eV for amorphous Mn doped $\text{Li}_2\text{B}_4\text{O}_7$ 50 uA of current, 1mm slit width, .1 integration time, and a -31°C PMT.

Photoemission Spectroscopy

In photoemission spectroscopy, monochromatic photons with enough energy to interact with the Mn doped $\text{Li}_2\text{B}_4\text{O}_7$ valence band and the inner core electrons, provided the energy necessary to overcome the work function of the material. These electrons were then emitted with a range of kinetic energies proportional to the valence band and inner core levels. Discussion of the photoemission data providing information on these core levels will be discussed in two stages. First, the TGM photoemission spectra obtained with incident 110 eV photons will be

discussed. Secondly, a closer look at the valence band and possible acceptor sites will be taken with the NIM system using lower photon energies.

TGM Photoemission Spectroscopy of Mn Doped $\text{Li}_2\text{B}_4\text{O}_7$

Photoemission spectra were taken with the TGM using 110 eV photons to allow comparison with the undoped $\text{Li}_2\text{B}_4\text{O}_7$ spectra and to determine energies associated with the Mn dopant. Initially, confirmation was required to ensure the photon was hitting the surface of the Mn doped $\text{Li}_2\text{B}_4\text{O}_7$ and not the tantalum wire used to secure the sample on the mount. Tantalum was used as a sample holder due to its known photoemission spectra and since it is a metal it provides the energy location for E_{fermi} . Figure 33 shows the kinetic energy versus intensity curve for the Ta wire and the Mn doped $\text{Li}_2\text{B}_4\text{O}_7$. The Mn doped $\text{Li}_2\text{B}_4\text{O}_7$ was confirmed with a second spectrum, the known spectrum for Ta, and compared to previous TGM photoemission work of undoped $\text{Li}_2\text{B}_4\text{O}_7$ as seen in Figure 34.

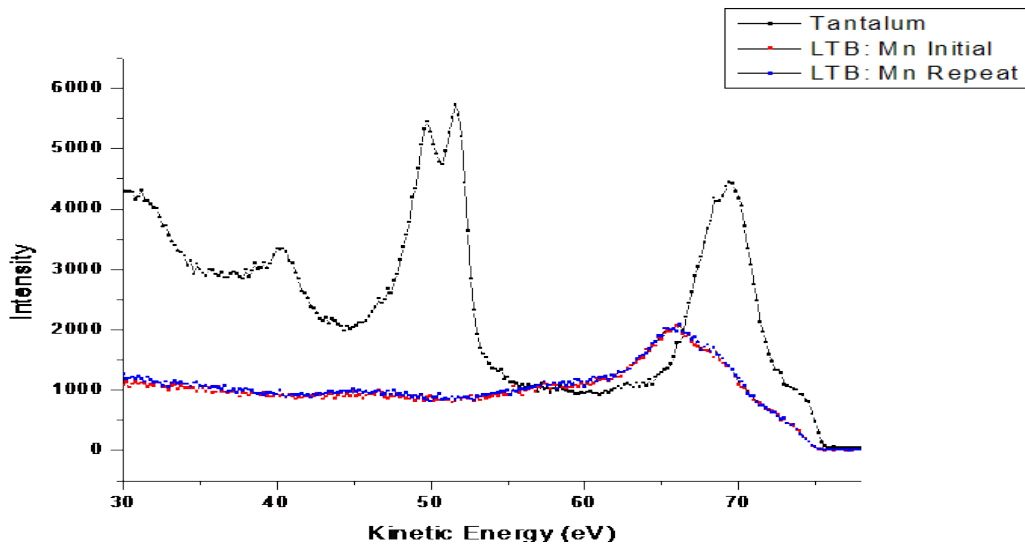


Figure 33. TGM photoemission spectra of tantalum wire and Mn Doped $\text{Li}_2\text{B}_4\text{O}_7$ with 95 eV photons at room temperature

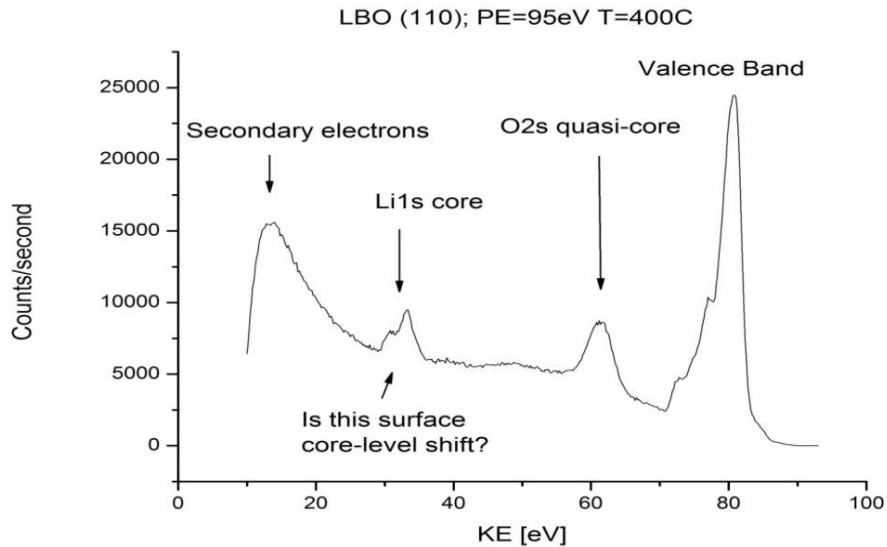


Figure 34. Photoemission spectra of undoped $\text{Li}_2\text{B}_4\text{O}_7$ with a TGM and 95 eV photons at 400 °C [4]

As a reference for analyzing this PES data, consider Figure 34. This plot shows a typical PES spectrum of undoped $\text{Li}_2\text{B}_4\text{O}_7$ mirroring the photoelectron energy spectra. The highest kinetic energy output is the valence band since valence band electrons require the least amount of photon energy to escape. The lowest level energy output is the core electron levels since they require most of the incoming photon energy to exit the crystal. This graph displays the Li 1s core, the secondary electrons, the O 2s core, and the valence band at 400K. Although O 2s is the nearest shallow core energy level to the valence band, this was not chosen as the primary reference point since it is very close to the valence band. Any suspected wave function interaction at lower level oxygen is more likely. Li has very little shift in the core and is the used reference point. [4]

Most often the spectra are published in terms of binding energy instead of kinetic energy to make uniform comparisons. If spectra were presented based on kinetic energy, one must know

the photon energy source used to collect data to compare the electrons in the sample with data collected using another source. The binding energy of the electron is equivalent to the energy of the photon less the work function of the material and less the kinetic energy of the electron. Throughout the TGM photoemission, 110 eV photons were used and the work function for $\text{Li}_2\text{B}_4\text{O}_7$ is approximately 4.3 eV. [4]

Literature reviews and previous publications have binding energy values for Li 1s at 54.7 eV, O 2s at 22.0 eV, and Mn 3p_{1/2} and 3p_{3/2} at 47.2 eV with an uncertainty of +/- 1 eV. [15] To ensure the Li 1s and O 2s core energy levels were correct, the core energy levels were compared against an absolute theoretical value using least squares fitting. [4] PES spectra obtained from Mn doped LTB are shown in Figure 35.

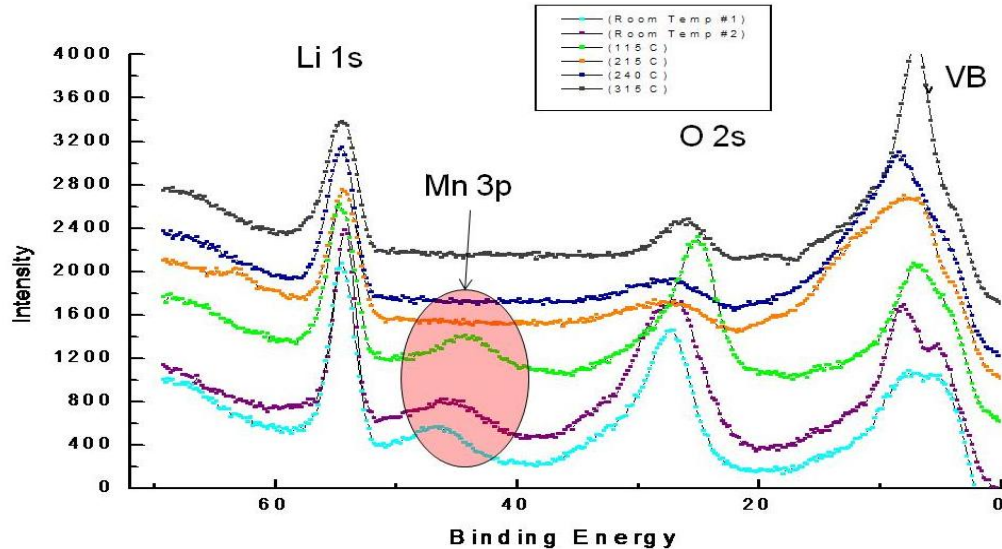


Figure 35. Binding energy versus intensity for Mn doped $\text{Li}_2\text{B}_4\text{O}_7$ with 110 eV photons at various temperatures

One sees that as the temperature increases, the photoemission peaks shift to the left. In the case of the valence band, the thermal energy helps mitigate the valence band shift by increasing the number of charge carriers and their mobility diminishing the positive surface charge. That is, the increase in temperature created thermal energy for electrons from deeper in the sample to move towards the empty orbitals near the surface of the sample. This mitigates the surface charging effect and provides spectra that are closer to ground state reality. It is, however, still necessary to adjust the raw spectra using both the Li 1s and O 2s core energy levels especially at low temperatures.

Again referring to Figure 35, one sees that as the temperature increases from room temperature to 215 °C the Mn peak disappears, whereas, when the sample was cooled from 240 to 115 °C the Mn peak reappeared. The Mn peak was only present below 115 °C. Also as the sample is heated, the surface charges and the valence band change. The O 2s levels are affected, but the deep Li 1s level remains quite constant since Li is an alkali metal, which, when singly ionized, possesses a noble gas configuration. The second ionization potential of lithium is thus quite high, due to the difficulty in removing any electron from an atom having a noble gas configuration. Hence, lithium atom 1s electrons are not easily ionized.

The photoemission spectra are in agreement with the cathodoluminescence spectra demonstrating a reduction in surface voltaic charge. As the photoemission spectra increase in temperature and then return to room temperature, the surface voltaic charging indicates only a little hysteresis even though this material is pyroelectric. In comparison with photoemission spectra from the undoped and Cu doped $\text{Li}_2\text{B}_4\text{O}_7$, the Mn doping appears to have suppressed the

charging and the pyroelectricity.[4] Since the Mn doped $\text{Li}_2\text{B}_4\text{O}_7$ has a (001) crystal orientation, i.e. the pyroelectric direction, and appears to produce less surface charging than the Cu and undoped $\text{Li}_2\text{B}_4\text{O}_7$, it may be the most promising dopant for a solid state neutron detector comprised of $\text{Li}_2\text{B}_4\text{O}_7$.[35]

Surface charging has resulted in a large photovoltaic charging problem with this oxide. Through photoemission an electron is freed from Mn doped $\text{Li}_2\text{B}_4\text{O}_7$ leaving behind a charged sample. Since charge is not mobile in an insulator, the photoemission effectively creates an immobile positive charge on the surface. These positive surfaces create a Columbic potential or space charge impacting photoelectrons moving towards the analyzer. This causes the spectrum to be shifted deeper in binding energy away from E_{Fermi} .

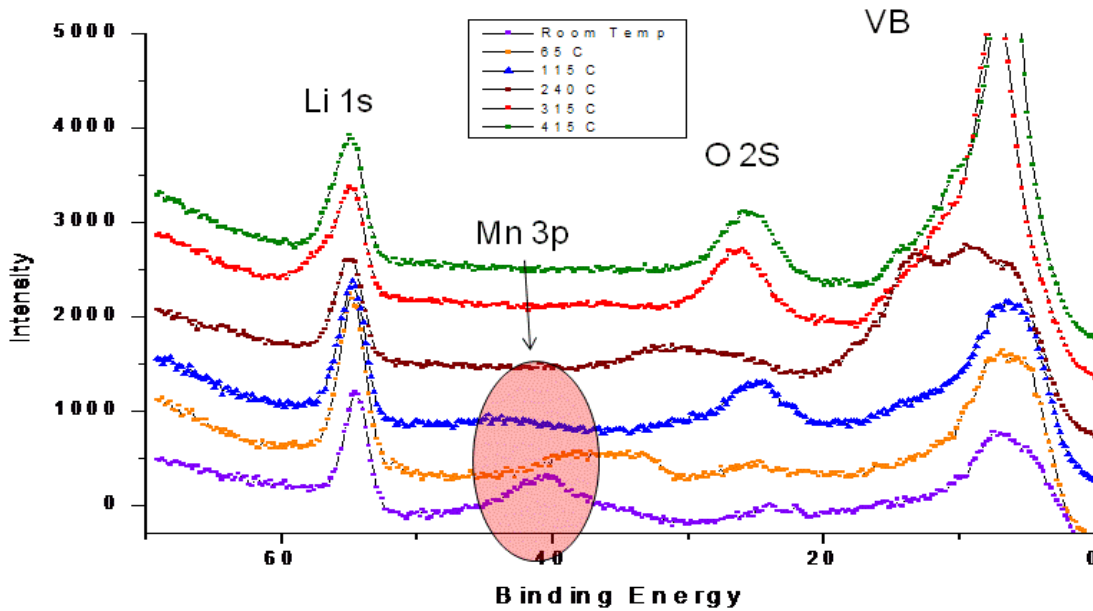


Figure 36. Binding energy versus intensity for Mn doped $\text{Li}_2\text{B}_4\text{O}_7$ with 110 eV photons at various temperatures after second sputter and annealing.

To further investigate the disappearance and reappearance of the Mn ions in the sample, the sample was cleaned a second time. The surface was sputtered with Ar atoms and annealed to 315 °C to remove surface impurities at the surface layers. The Mn was again present after the second cleaning of the crystal's surface and as can be seen from Figure 36, the Mn was apparent at low temperatures. The sample was brought to 350 °C to see if a higher temperature is required to get the surface reestablished after sputtering. Photoemission spectra were obtained at room temperature, 315, 214, 215, and 115 °C respectively. At room temperature, the Mn feature was present at 47.2 eV, but again it disappeared and was only restored when the temperature was finally lowered to 115 °C. The Mn and O disappeared, but when Mn reappeared it was at a different binding energy than before cooling. The Mn ions segregate on the surface at low temperatures and dissolve into the bulk of the material at the higher temperatures. [35]

NIM Photoemission Spectroscopy of Mn Doped Li₂B₄O₇

Photoemission spectra were taken using the NIM beamline with a 0.01 degree resolution Scienta energy analyzer providing an energy resolution of approximately 10 meV for photons with incident energies varying from 24 to 32 eV. The purpose of the NIM measurements was to examine the region of the valence band edge to the center of the bandgap. At these energies, the photons can only excite transitions from the acceptor states of Mn doped Li₂B₄O₇ near the valence band.

In the preparatory chamber, the Mn doped Li₂B₄O₇ was heated to 200 °C and sputtered with an argon gas at 21 V and 380 mA for 15 minutes to clean the surface. Spectra were then taken from the Mn doped Li₂B₄O₇ at various temperatures using 27 eV photons. A like spectrum

was taken from a gold sample. Since Au is a metal it was utilized to calibrate the system for E_{fermi} at 23.25 eV. Figure 36 is an intensity versus kinetic energy graph for Mn doped $\text{Li}_2\text{B}_4\text{O}_7$ using 27 eV photons at various temperatures. These spectra are compared to the Au spectrum to establish E_{fermi} . As represented in Figure 37, surface charging reduced as the temperature was increased to 200 °C, the maximum temperature allowed with the NIM system.

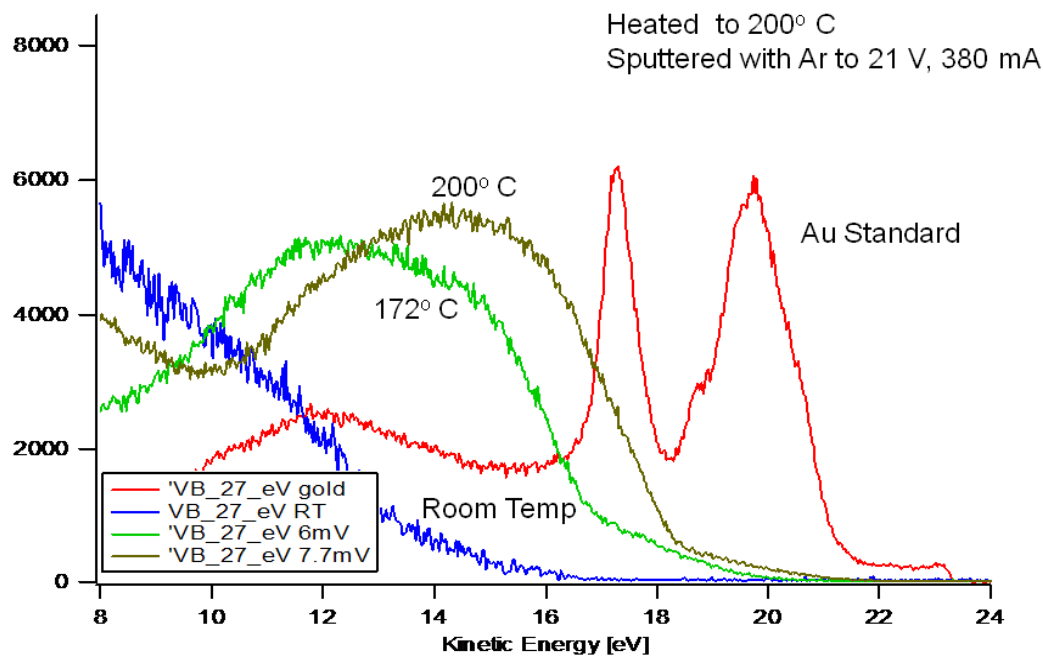


Figure 37. NIM Photoemission spectra at 27 eV at various temperatures

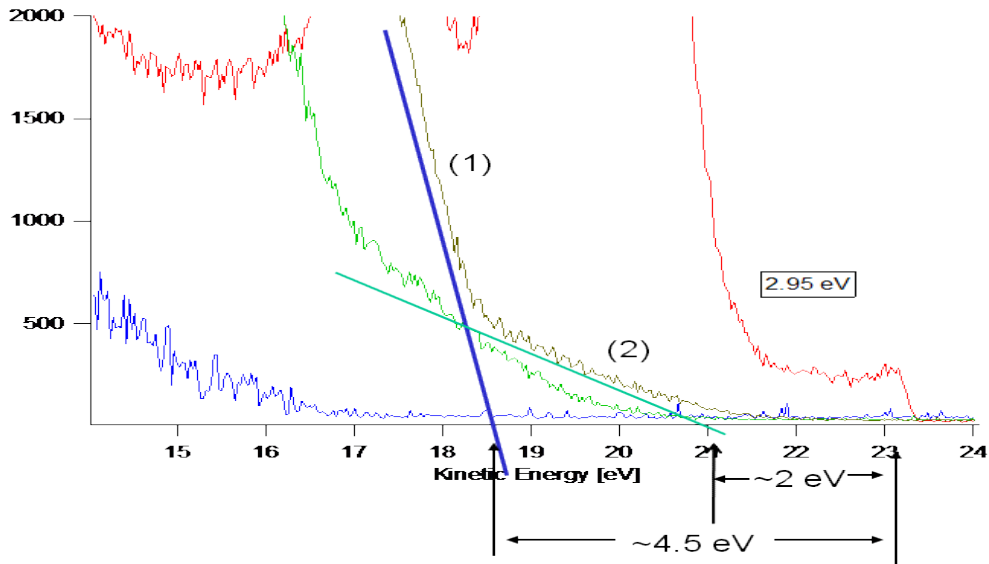


Figure 38. Efermi, Ev, and surface states for Mn doped $\text{Li}_2\text{B}_4\text{O}_7$

Figure 38 is an enlarged section of Figure 37 which shows a detailed representation of the band gap of Mn doped $\text{Li}_2\text{B}_4\text{O}_7$. The valence band edge is at approximately 18.75 eV and E_{fermi} is approximately 23.25 eV, representing a difference of approximately 4.5 eV and is representative only of the atom layers closest to the surface. Surface states are responsible for the energy tail from 18.75 eV to 21.25 eV followed by an unoccupied bandgap region of 2 eV. This approximation of an energy difference of 4.5 eV from E_v to E_{fermi} is in basic agreement with a band gap of 9.5 eV. [4]

Since 200 °C was determined to be the best temperature to reduce charging within the limits of our system, Figure 39 is the intensity versus kinetic energy graph for Mn doped $\text{Li}_2\text{B}_4\text{O}_7$ which was obtained by maintaining a constant temperature and varying the photon energy. As the photon energy was reduced by 2 eV, the corresponding E_v was shifted to 2 eV less in kinetic

energy. A photon energy of 26 eV was then selected to perform a detailed scan of the valence band region using a 20 meV step size.

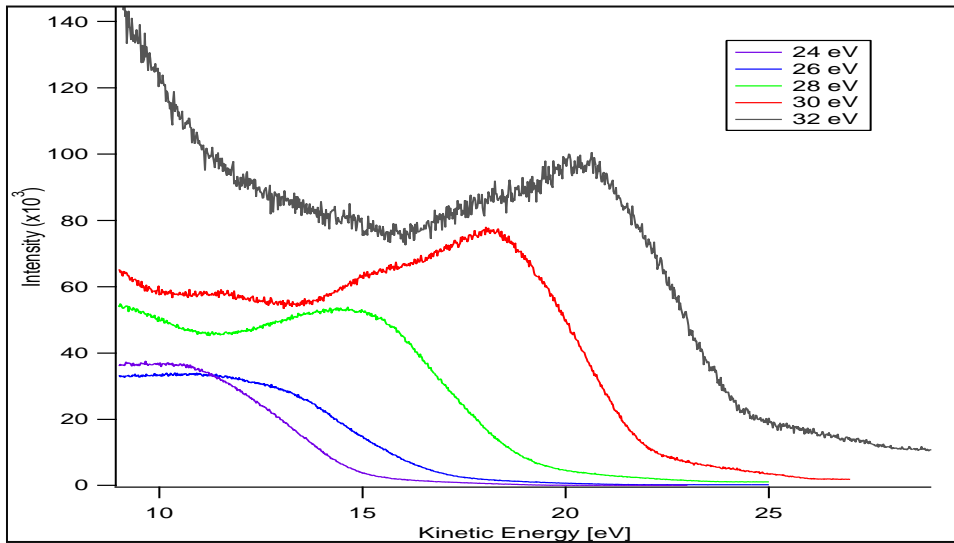


Figure 39. NIM PES of Mn doped $\text{Li}_2\text{B}_4\text{O}_7$ at 200°C and photon energies ranging from 24-32 eV.

Figure 40 is the resulting intensity versus kinetic energy graph. As was stated earlier, this long, detailed scan was conducted to see if any acceptor states were present. As can be seen from the data, no clearly discrete acceptor states were found; the only possible acceptor states would be located above 17.75 eV, a region of the PES curve which is very smooth. As was stated earlier, the smooth structure in this region is probably due to surface states.

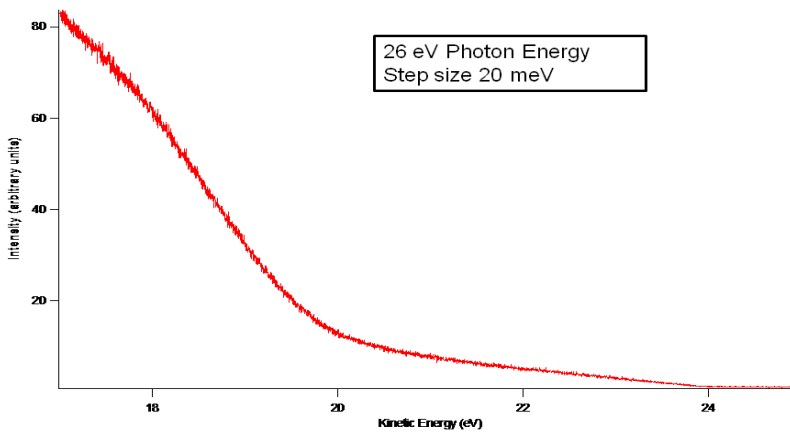


Figure 40. NIM PES spectra with 26 eV photon energy at 20 meV step size.

Finally, a temperature dependent scan was conducted at 26 eV photon energy to determine what sample temperature is required to adequately reduce the surface charging of the Mn doped $\text{Li}_2\text{B}_4\text{O}_7$. Figure 41 represents the intensity versus kinetic energy curve of Mn doped $\text{Li}_2\text{B}_4\text{O}_7$ at various temperatures. As can be seen in Figure 41 below, charging was significantly reduced at temperatures greater than 122 °C. This reduction in charging is believed to be due to the presence of Mn in the crystal.

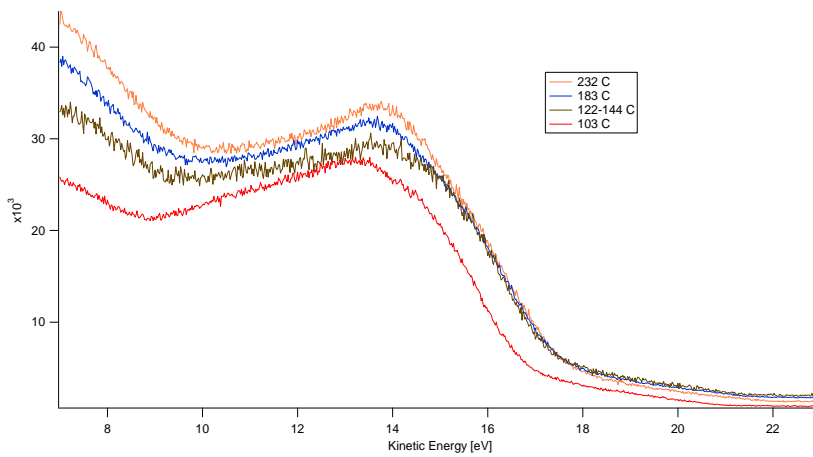


Figure 41. Temperature Dependent NIM PES Spectra with 26 eV photon energy.

Discussion

Conclusion of Research

This research was conducted to satisfy three goals; (1) to acquire a better understanding of the states present in the energy bandgap of undoped and Mn doped $\text{Li}_2\text{B}_4\text{O}_7$ using cathodoluminescence spectroscopy, (2) to study the bulk states of Mn doped $\text{Li}_2\text{B}_4\text{O}_7$ and confirm the presence of Mn utilizing low resolution photoemission spectroscopy, and (3) to investigate potential acceptor states near the valence band edge of Mn doped $\text{Li}_2\text{B}_4\text{O}_7$'s using high resolution photoemission spectroscopy.

Although the original goal of obtaining cathodoluminescence spectra across the full 9.5 eV bandgap was not realized due to equipment problems, the spectra obtained did provide evidence of self trapped excitons in both the undoped and Mn doped $\text{Li}_2\text{B}_4\text{O}_7$. In addition, the narrowing of the primary cathodoluminescence peak around 3.7 eV in the Mn doped $\text{Li}_2\text{B}_4\text{O}_7$ confirmed that Mn doping increases the conductivity of $\text{Li}_2\text{B}_4\text{O}_7$ enhancing its potential as a solid state neutron detector.

The TGM (low resolution) photoemission spectroscopy was paramount to this study as it was these measurements that confirmed the presence of Mn in the samples. This important identification was the result of the presence of a peak in the PES spectra at a binding energy of 47.2 eV. Interestingly, the Mn ions were found to segregate to the surface at low temperatures and dissolve into the bulk of the material at the higher temperatures.

The NIM (high resolution) photoemission spectroscopy established the presence of surface states but revealed no acceptor states. Also, there is strong indication that the presence of

Mn in the Mn doped sample suppressed the charging seen in the photoemission data of the undoped $\text{Li}_2\text{B}_4\text{O}_7$. As a result, the Mn doped $\text{Li}_2\text{B}_4\text{O}_7$ displayed minimal charging effects in photoemission after the temperature was raised to approximately 130°C once again confirming that the Mn dopant may be a suitable initial choice in the production of a solid state neutron detection device.

Recommendations for Future Research

There are several directions in which the research presented in this thesis on undoped and Mn doped $\text{Li}_2\text{B}_4\text{O}_7$ could be continued and expanded. First and foremost, cathodoluminescence of Mn doped $\text{Li}_2\text{B}_4\text{O}_7$ into the VUV will allow all transitions within the bandgap to be explored. This data is necessary to complete the band mapping of the crystal. Complementing this research would be the inverse photoemission spectroscopy of Mn doped $\text{Li}_2\text{B}_4\text{O}_7$. Inverse photoemission spectroscopy would provide band mapping from E_{fermi} to the conduction band and thus provide confirmation of the data obtained from cathodoluminescence, and thus provide a complete band mapping of the Mn doped $\text{Li}_2\text{B}_4\text{O}_7$.

Another major contribution to this project would photon dependent photoemission spectroscopy to look for resonant photoemission of Li 1s and Mn 3p at elevated temperatures. Since Mn dissolves back into the bulk, the resonant photoemission would determine what part of the valence band is hybridized to the Mn. Finally, angle resolved photoemission spectroscopy, ARPES, of Mn doped $\text{Li}_2\text{B}_4\text{O}_7$ would reaffirm the presence of surface states in the valence band of the crystal.

Finally, electron paramagnetic resonance spectroscopy would provide useful information to characterize point defects in as grown Mn doped Li₂B₄O₇ crystals. Characterization of point defects would provide information on crystal defects and confirm mechanisms producing the cathodoluminescence spectra.

Bibliography

- [1] M. Swinney, Defect Characterization, Scintillation Properties, and Neutron Detection Feasibility of Lithium Tetraborate, 2010.
- [2] J.L. Jones, Detection of Shielded Nuclear Material in a Cargo Container, June 2005.
- [3] John W. McClory, Uranium and Gadolinium Semiconductors for Next-Generation Solid-State Neutron Detectors, 2010.
- [4] Alan Munter. (2003, October) NIST Center for Neutron Research. [Online].
<http://www.ncnr.nist.gov/resources/n-lengths/>
- [5] David J. Wooten, "Electronic Structure of Lithium Tetraborate," Air Force Institute of Technology, Wright Patterson AFB, 2010.
- [6] Glenn F. Knoll, *Radiation Detection and Measurement*. New York: John Wiley & Sons, Inc, 1988.
- [7] Mazharul M. Islam, Volodymyr V. Maslyuk, Thomas Bredow, and Christian Minot, "Structural and Electronic Properties of Li₂B₄O₇," *J. Phys. Chem. B.*, vol. 109, pp. 13597-13604, 2005.
- [8] B. V. Padlyak, Y. V. Burak, and V. M. Shevel, "Neutron -Induced Defects in the Lithium Tetraborate Single Crystals," *Radiation Effects & Defects in Solids*, pp. 1101-1109, 2002.
- [9] V. Holovey, V. Sidey, V. Lyamayev, and M. Birov, "Influence of different annealing conditions on the luminescent properties of Li₂B₄O₇:Mn Single Crystals," *Journal of Physics and Chemistry of Solids*, vol. 68, pp. 1305-1310, 2007.
- [10] Ya Burak, V. Adamiv, I. Teslyuk, and V. Shevel, "Optical Absorption of Isotopically enriched Li₂B₄O₇ Single Crystals Irradiated by Thermal Neutrons," *Radiation*

Measurements, vol. 38, pp. 681-684, 2004.

- [11] Tallant D.R., Warren W.L. Seager C.H., "Cathodoluminescence, Reflectivity Changes, and Accumulation of Graphitic Carbon during Electron Beam Aging of Phosphors," *J.Appl.Phys.*, vol. 82, p. 4515, August 1997.
- [12] Olympus Corporation. (2004-2009) Semiconductor Diode Lasers. [Online].
<http://www.olympusfluoview.com/java/diodelasers/index.html>
- [13] B. G. Yacobi, *Cathodoluminescence Microscopoy of Inorganic Solids*. New York: Plenum Press, 1990.
- [14] D. R. Vij, *Luminenscence of Solids*. New York: Plenum Press, 1998.
- [15] Mark Fox, *Optical Properties of Solids*. New York: Oxford University Press, 2010.
- [16] Stefan Hufner, *Photoelectron Spectroscopy Principles and Applications*. New York: Springer, 2003.
- [17] John P. McKelvey, *Solid State Physics*. Malabar, Floriday: Krieger Publishing Company, 1993.
- [18] A. Kuznetsov, A. Krushalov, I. Ogorodnikov, and A. Sobolev, "Electronic Structure of Lithium Tetraborate Li₂B₄O₇ Crystals. Cluster Calculations and X-ray Photoelectron Spectroscopy," *Physics of the Solid State*, vol. 41, no. 1, January 1999.
- [19] I. Ogorodnikov, V. Yakovlev, A. Krushalov, and L. Isaenko, "Transient Optical Absorption and Luminenscence in Li₂B₄O₇ Lithium Tetraborate," *Physics of the Solid State*, vol. 44, no. 6, pp. 1085-1092, 2002.
- [20] D. Podgorska, S. Kacmarek, and W. Drozdowski, "Growth and Optical Properties of Li₂B₄O₇ Single Crystals Pure and Doped with Yb, Co and Mn Ions for Nonlinear

Applications," *Acta Physica Polonica A*, vol. 107, no. 3, pp. 507-518, 2005.

- [21] M. Ignatovych, V. Holovey, T. Vidoczy, P. Baranyai, and A. Kelemen, "Spectral Study on Manganese and Silver Doped Lithium Tetraborate Phosphors," *Radiation Physics and Chemistry*, vol. 76, pp. 1527-1530, 2007.
- [22] A. Kelemen, M. Ignatovych, V. Holovey, T. Vidoczy, and P. Baranyai, "Effect of Irradiation on Photoluminescence and Optical Absorption Spectra of Li₂B₄O₇:Mn and Li₂B₄O₇:Ag Crystals," *Radiation Physics and Chemistry*, vol. 76, pp. 1531-1534, 2007.
- [23] V. Adamiv, V. Savchyn, P. Savchyn, I. Teslyuk, and Ya. Burak, "Influence of Isovalent Doping on the Cathodoluminescence of Li₂B₄O₇:A (A=K,Cu,Ag) Single Crystals," *Functional Materials*, vol. 16, no. 3, pp. 247-252, 2009.
- [24] Judith L. McFall, "Cathodoluminescence of AlGaN," Air Force Institute of Technology, Wright Patterson AFB , 2000.
- [25] Christopher Palmer. (2005, January) PLANE GRATINGS AND THEIR MOUNTS. [Online]. <http://gratings.newport.com/information/handbook/chapter6.asp#6.2>
- [26] (1996-2010) Horiba Scientific. [Online]. <http://www.horiba.com/scientific/products/gratings/catalog/ruled-plane-gratings/grating-list/>
- [27] C. M. Evans, J. D. Scott, and E. Morikawa, "The Double-Tailed Normal Incidence Monochromator Beamline at CAMD," *Review of Scientific Instruments*, vol. 73, p. 1557, 2002.
- [28] Dominique Drouin et al., "A Fast and Easy-to-use Modeling Tool for Scanning Electron Microscopy and Microanalysis Users," *Scanning*, vol. 29, pp. 92-101, 2007.
- [29] Brandt Kananen, 2010, Personal Correspondence.

- [30] S. Tretiak, A. Saxena, R. L. Martin, and A. R. Bishop, "Photoexcited Breathers in Conjugated Polyenes: An Excited-State Molecular Dynamics Study," Theoretical Division and Center for Nonlinear Studies Los Alamos National Laboratory, Los Alamos, 2002.
- [31] I. N. Ogorodinkov et al., "Self-Trapped Excitons in LiB₃O₅ and Li₂B₄O₇ Lithium Borates: Time-Resolved Low-Temperatures Luminescence VUV Spectroscopy," *Physics of the Solid State*, vol. 42, no. 3, pp. 464-472, 2000.
- [32] R. T. Williams and K. T. Song, "The Self-Trapped Exciton," *J. Phys. Chem. Solids*, vol. 51, no. 7, pp. 679-716, 1990.
- [33] R. T. Williams and K. S. Song, "The Self-Trapped Exciton," *J. Phys. Chem. Solids*, vol. 51, no. 7, pp. 679-716, 1990.
- [34] Volodymyr T. Adamiv et al., "The Electronic Structure and Secondary Pyroelectric Properties of Lithium Tetraborate," *Materials*, vol. 3, pp. 4550-4579, 2010.
- [35] Peter Dowben , 2010, Personal Correspondence.
- [36] R.J. Nikolic, Future of Semiconductor Based Thermal Neutron Detectors, February 2006.
- [37] Richard Kouzes, Passive neutron detection for interdiction of nuclear material at borders.
- [38] Marsbed H. Hablanian, *High-Vacuum Technology A Practical Guide*. New York: Marcel Dekker, Inc., 1997.
- [39] Tallant D.R., Warren W.L. Seagar C.H., "Surface Charging of Phosphors and its Effects on Cathdoluminescence at Low Electron Energies," Sandia National Laboratories, Albuquerque,,

- [40] Siciliano E.R., Ely J.H., Keller P.E., McConn R.J. Kouzes R.T., "Passive Neutron Detection for Interdiction of Nuclear Material at Borders," *Nuclear Instruments and Methods in Physics Research A*, vol. 584, pp. 383-400, 2008.
- [41] Richard Kouzes, "Passive Neutron Detection for Interdiction of Nuclear Material at Borders," Pacific Northwest National Laboratory, Richland, 2007.
- [42] A. Munster. (2003, October) Neutron Scattering Lengths and Cross Sections. NIST Center for Neutron Research. [Online]. <http://www.ncnr.nist.gov/resources/n-lengths/>
- [43] H. Winich, *Synchrotron Radiation Sources: A Primer*. River Edge, New Jersey: World Scientific Publishing Co. Ltd., 1995.
- [44] M. Cardona and Peter Yu, *Fundamentals of Semiconductors: Physics and Material Properties*. New York: Springer, 2005.

Vita

Major Christina Dugan hails from York, PA and is a graduate of the United States Military Academy with a Bachelor of Science Degree in Chemistry/Life Science and a minor in Nuclear Engineering. Upon graduation she was commissioned as a Second Lieutenant in May 2000.

MAJ Dugan's first assignment was in the 10th Mountain Division, Fort Drum, New York. She was a platoon leader in the 514th Maintenance Company and in B Company, 710th Main Support Battalion. Her next assignments were the battalion supply officer and battalion adjutant in the 710th Main Support Battalion. Following these assignments she moved to New Cumberland, PA and was the aide-de-camp to the Commander of the Defense Distribution Center from July 2003 to July 2005. In July 2005, she was a student officer, U.S. Army Logistics Management College, Fort Lee, Virginia. Returning to Fort Drum in January 2006, she deployed in 10th Sustainment Brigade as a logistical planner for the Joint Logistics Command in Bagram, Afghanistan. From November 27, 2006 to May 2008 she commanded of Alpha Company, 277th Aviation Support Battalion, 10th Combat Aviation Brigade, 10th Mountain Division, and Fort Drum, New York.

MAJ Dugan's military education includes: Ordnance Officer Basic Course, Combined Logistics Officer Career Course, Army's FA-52 course, Air Assault, Unit Movement Officers Course, Master Fitness Course, and Combat Life Saver Course.

Her awards include: Joint Commendation Medal (2 OLC), Army Commendation Medal, Army Achievement Medal (1 OLC), Joint Meritorious Unit Award, Army Superior Unit Award (1 OLC), National Defense Medal, Global War on Terrorism Medal, Afghanistan Campaign Medal, Army Service Ribbon, the Combat Action Badge, and the Air Assault Badge.

REPORT DOCUMENTATION PAGE

*Form Approved
OMB No. 074-0188*

The public reporting burden for this collection of information is estimated to average 1 hour per response, including the time for reviewing instructions, searching existing data sources, gathering and maintaining the data needed, and completing and reviewing the collection of information. Send comments regarding this burden estimate or any other aspect of the collection of information, including suggestions for reducing this burden to Department of Defense, Washington Headquarters Services, Directorate for Information Operations and Reports (0704-0188), 1215 Jefferson Davis Highway, Suite 1204, Arlington, VA 22202-4302. Respondents should be aware that notwithstanding any other provision of law, no person shall be subject to a penalty for failing to comply with a collection of information if it does not display a currently valid OMB control number.

PLEASE DO NOT RETURN YOUR FORM TO THE ABOVE ADDRESS.

1. REPORT DATE (DD-MM-YYYY) 24-03-2011			2. REPORT TYPE Master's Thesis		3. DATES COVERED (From – To) March 2010-March 2011
4. TITLE AND SUBTITLE Cathodoluminescence and Photoemission of Undoped and Mn Doped Lithium Tetraborate					5a. CONTRACT NUMBER
					5b. GRANT NUMBER
					5c. PROGRAM ELEMENT NUMBER
6. AUTHOR(S) Dugan, Christina L., MAJ, USA					5d. PROJECT NUMBER
					5e. TASK NUMBER
					5f. WORK UNIT NUMBER
7. PERFORMING ORGANIZATION NAMES(S) AND ADDRESS(S) Air Force Institute of Technology Graduate School of Engineering and Management (AFIT/EN) 2950 Hobson Way WPAFB OH 45433-7765					8. PERFORMING ORGANIZATION REPORT NUMBER AFIT/GNE/ENP/11-M05
9. SPONSORING/MONITORING AGENCY NAME(S) AND ADDRESS(ES) Defense Threat Reduction Agency COL Mark Mattox 1900 Wyoming Blvd SE Kirtland AFB, NM 87117-5669					10. SPONSOR/MONITOR'S ACRONYM(S) DTRA/OP-CSU
					11. SPONSOR/MONITOR'S REPORT NUMBER(S)
12. DISTRIBUTION/AVAILABILITY STATEMENT <u>APPROVED FOR PUBLIC RELEASE; DISTRIBUTION UNLIMITED</u>					
13. SUPPLEMENTARY NOTES					
14. ABSTRACT Lithium tetraborate ($Li_2B_4O_7$) crystals are being developed for possible use in solid state neutron detectors. The $^6Li(n,\alpha)^3H$ and $^{10}B(n,\alpha)^7Li$ reactions are the basis for neutron detection, and a $Li_2B_4O_7$ crystal enriched with Mn should show improved efficiency for neutron detection. There is a lack of fundamental characterization information regarding this useful material, particularly with regard to its electronic configuration. Photoemission spectroscopy was used to determine the energy level structure of the Mn doped $Li_2B_4O_7$ crystals. Measurements were made using ultraviolet photoemission spectroscopy (UPS) using synchrotron radiation on two different beamlines. The first was the 3 m toroidal grating monochromator (TGM) beam line confirming the presence of Mn. Secondly, the normal incident monochromator (NIM) beamline studied the band gap states. Measurements were made at elevated sample temperatures to reduce charging effects. Photoemission studies provided evidence of Mn in the bulk crystal at 47.2 eV. Valence band analysis provided the presence of surface states but no acceptor sites. Cathodoluminescence studies were performed on undoped and Mn doped at beam energies from 5 to 10 KeV and at room temperature. Self trapped exciton emission states are evident in the undoped and Mn doped $Li_2B_4O_7$ sample ranging in energies from 3.1 to 4.1 eV.					
16. SECURITY CLASSIFICATION OF:		17. LIMITATION OF ABSTRACT UU	18. NUMBER OF PAGES 101	19a. NAME OF RESPONSIBLE PERSON Dr. Robert Hengehold (AFIT/ENP)	
a. REPORT U	b. ABSTRACT U			c. THIS PAGE U	19b. TELEPHONE NUMBER (Include area code) (937)785-3636 ext. 4502

Standard Form 298 (Rev. 8-98)

Prescribed by ANSI Std. Z39-18